

# Magnetic Tunable Microstructured Surfaces for Thermal Management and Microfluidic Applications

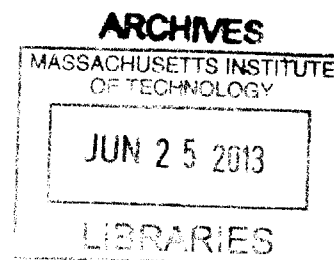
by

Yangying Zhu

SUBMITTED TO THE DEPARTMENT OF MECHANICAL ENGINEERING IN  
PARTIAL FULFILLMENT OF THE REQUIREMENTS FOR THE DEGREE OF

MASTER OF SCIENCE IN MECHANICAL ENGINEERING  
AT THE  
MASSACHUSETTS INSTITUTE OF TECHNOLOGY

June 2013



©2013 Massachusetts Institute of Technology. All rights reserved.

Signature of Author: \_\_\_\_\_  
Department of Mechanical Engineering  
May 10, 2013

Certified by: \_\_\_\_\_  
Evelyn N. Wang  
Associate Professor of Mechanical Engineering  
Thesis Supervisor

Accepted by: \_\_\_\_\_  
David Hardt  
Professor of Mechanical Engineering  
Chairman, Graduate Thesis Committee



# **Magnetic Tunable Microstructured Surfaces for Thermal Management and Microfluidic Applications**

By

**Yangying Zhu**

Submitted to the Department of Mechanical Engineering  
On May 10, 2013 in partial fulfillment of the  
Requirements for the Degree of Master of Science in  
Mechanical Engineering

## **Abstract**

Micro and nanostructured surfaces have broad applications including heat transfer enhancement in phase-change systems and liquid manipulation in microfluidic devices. While significant efforts have focused on fabricating static micro/nanostructured arrays, uniform arrays that can be dynamically tuned have not yet been demonstrated. In this work, we present a novel fabrication process for magnetically tunable microstructured surfaces, where the tilt angle can be controlled upon application of an external magnetic field. We also demonstrated this platform for droplet manipulation in heat transfer applications.

The tunable surfaces consist of ferromagnetic nickel (Ni) pillars on a soft PDMS substrate. The pillars have diameters of 23-35  $\mu\text{m}$ , pitches of 60-70  $\mu\text{m}$ , and heights of 70-80  $\mu\text{m}$ . We used vibrating sample magnetometry to obtain hysteresis loops of the Ni pillar arrays which match well the properties of bulk Ni. With a field strength of 0.5 tesla and a field angle of  $60^\circ$ , a uniform  $10.5 \pm 1^\circ$  tilt angle of the pillar arrays was observed.

Furthermore, we developed a model to capture the tilt angle as a function of the magnetic field, and showed that by replacing nickel to cobalt, the tilt angle could be increased to  $30^\circ$  with the same field. Meanwhile, simulations show good agreement with the experiments. Future work will focus on using these surfaces to actively transport water droplets and spread the liquid film *via* pillar movement. This work promises tunable surface designs for important device platforms in microfluidics, biological and optical applications.

Thesis Supervisor: Evelyn N. Wang  
Title: Associate Professor of Mechanical Engineering





## **Acknowledgements**

This work could not have been possible without the help and support from many people that I am so fortunate to have in my life.

I would like to gratefully acknowledge the help and support of my advisor Professor Evelyn Wang, whose guidance and insight truly inspired me throughout the past two years to complete this work.

I would also like to acknowledge Dr. Xiao Rong, Dr. Kuang-Han (Hank) Chu and all the other students, postdocs and alumni in the Device Research Laboratory, who provided inspiring ideas and guidance in completing this work. I also gratefully acknowledge funding support from the Air Force Office of Scientific Research (AFOSR), and Microsystems Technology Laboratories at the Massachusetts Institute of Technology for fabrication staff support, help, and use of equipment.

Finally, thank you to my dear and loving parents.



## Contents

Abstract .....	3
Contents .....	7
1. Introduction.....	9
1.1 Micro/Nanostructured Surfaces and their applications.....	9
1.2 Asymmetric and Static Tunable Surfaces .....	10
1.3 Dynamically Tunable Surfaces .....	11
2. Design of Magnetically Tunable Surfaces .....	13
2.1 Surface Designs .....	13
Design 1: Embed Magnetic Particles into Cellulose Nanofibrils templates .....	13
Design 2: Machining Composite Magnetic Material into Micropillar Arrays .....	17
Design 3: Electroplating magnetic pillars attached to soft substrate .....	18
2.2 Fabrication to realize tunable surfaces.....	19
3. Characterizing and Testing .....	25
3.1 Characterizing Magnetization .....	25
3.2 Tilt angle Testing .....	26
4. Simulation and Modeling.....	29
4.1 Mechanical deflection simulation .....	29
4.2 Magnetic torque .....	33
5. Discussions .....	39
5.1 Surface interaction with water droplets.....	39
5.2 Directions for the future.....	41
6. Conclusion .....	45
Bibliography .....	46
Appendix: Calculation of deflection angle of microstructured surfaces fabricated from bacteria cellulose nanofibrils embedded with magnetic nanoparticles .....	48

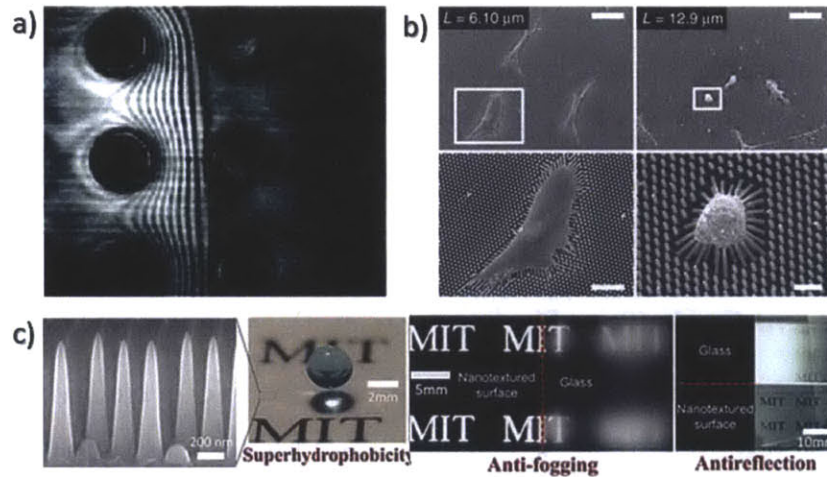
## List of Figures

Figure 1 Micro/nanostructured surfaces and their applications.....	9
Figure 2 Schematics showing the concept of magnetically tunable micropillar arrays.....	12
Figure 3 Design and fabrication of cellulose nanofibrils embedded with cobalt ferrite magnetic nano particles .....	14
Figure 4 Deflection angle as a function of external magnetic field and aspect ratio .....	16
Figure 5 Magnetic microstructured surfaces fabricated with composite materials .....	18
Figure 6 Schematic showing mechanism of design 3 .....	19
Figure 7 Fabrication process flow for magnetically tunable micropillar arrays.....	19
Figure 8 SEMs of fabricated tunable micropillars with diameters of 24-27 $\mu\text{m}$ , heights of 60-80 $\mu\text{m}$ , and spacings of 60 $\mu\text{m}$ .....	20
Figure 9 SEMs of photoresist mold on Au seed layer .....	21
Figure 10 Samples and electroplating setup. ....	22
Figure 11 Electroplated nickel detachment and photoresist residues. ....	23
Figure 12 Kapton tape aided transferring method .....	24
Figure 13 In-plane and out-of-plane magnetic hysteresis loop of the electroplated nickel pillar arrays on a silicon substrate. ....	25
Figure 14 Tilt angle testing setup.....	27
Figure 15 Experimental demonstration of tilted pillars .....	27
Figure 16 Finite element simulation a unit cell with dynamic load.....	30
Figure 17 Displacement difference in the x-direction between top pillar surface and bottom pillar surface as a function of time .....	31
Figure 18 Schematic of boundary conditions and load of the model .....	31
Figure 19 Finite element (Abaqus) simulation of tilt angle as a function of mechanical torque..	32
Figure 20 Finite element simulation of tilt angle.....	33
Figure 21 A magnetic micropillar placed inside a magnetic field .....	34
Figure 22 Calculation of magnetic torque as a function of tilt angle. Field angle was $60^\circ$ .....	35
Figure 23 Equilibrium point determined by intersection of mechanical and magnetic torque.....	35
Figure 24 Simulation result of tilt angle as a function of field strength. ....	36
Figure 25 Partially wetting liquid sitting on the fabricated magnetically tunable surfaces. ....	39
Figure 26 A Wenzel state droplet and detachment of the nickel pillars .....	40
Figure 27 A fabricated surface before wetting and after wetting. ....	41
Figure 28 Schematic of tilt angle testing stage. ....	43

# 1. Introduction

## 1.1 Micro/Nanostructured Surfaces and their applications

Micro and nanostructured surfaces have broad applications ranging from liquid transport in microfluidics, cell manipulation in biological systems, to light tuning in optical applications. For example, Xiao *et al.* have investigated microscopic sweeping behavior of liquid film front spreading on hydrophilic micropillar arrays which plays the key role in passive thin film evaporation heat transfer applications (Figure 1a) [1]. Elastomeric PDMS micropillar arrays with tunable rigidity have been demonstrated to impact cell morphology, adhesions, contractility and stem cell differentiation (Figure 1b) [2]. Park *et al.* have developed nanostructured silica surface as a superhydrophobic, anti-fogging and anti-reflective multi-functional surface (Figure 1c) [3].



**Figure 1** Micro/nanostructured surfaces and their applications. a, Interference microscopy image of the liquid meniscus sweeping between pillars, adapted from [1]. b, Scanning electron micrographs of hMSCs cell placed on PDMS micropost arrays, adapted from [2]. c, Nanotextured silica surface with superhydrophobic, anti-fogging and anti-reflection properties, adapted from [3].

Particularly, with the recent development of surface engineering, microstructured surfaces have brought significant opportunities to enhance phase change heat transfer in thermal management for applications such as electronic device cooling, steam condensation in power plant and temperature control in solar cells. There has been increasing interest to use micro/nanostructured surfaces to enhance condensation, evaporation and boiling heat transfer performance. For example, microscale roughened surfaces have been experimentally demonstrated as well as theoretically explained to enhance pool boiling heat transfer, increasing critical heat flux (CHF) to over  $200 \text{ W/cm}^2$  [4][5]. CHF of  $230 \text{ W/cm}^2$  has been reported on

hierarchically structured surfaces of silicon micro pillar arrays covered with ZnO nanowires [6]. Micro copper arrays covered with copper oxide nanostructures could further enhance CHF to  $250 \text{ W/cm}^2$ , which highlighted the important role of roughness using structures at multiple length scales for CHF enhancement [7]. In flow boiling experiments, researchers have found that introducing silicon nanowires into microchannel can significantly reduce pressure and temperature fluctuation caused by rapid vapor bubble growth [8]. The increased nucleation density introduced from the nanostructures reduced flow instability, which is a challenging problem associated with the flow boiling cooling device. Micro cavities and inlet flow restrictors of multi-microchannels have also been shown to increase stability by enhancing bubble nucleation as well as generating a pressure drop across the inlet, resulting in a direct transition from single phase to a stable slug flow in the channel [9]. Micro/Nano roughened surfaces also significantly enhanced condensation heat transfer performance by increasing nucleation sites and facilitate droplets removal [10]. In loop heat pipe devices the micro wick structures introduce capillary driven flow, providing passive pumping to reduce pumping energy cost. The structures can also expand thin film evaporation area to enhance evaporation heat transfer [11].

## ***1.2 Asymmetric and Static Tunable Surfaces***

While researchers have focused on static and isotropic micro/nanostructures, recent studies extended the idea to asymmetric and anisotropic surfaces for various applications. For example, with the help of deflected pillar arrays on the surface, liquid can spread in one direction while pinned in other directions. The deflection angle of the nanostructures can be tuned in this case to achieve different liquid spreading behavior [12]. These surfaces can not only drive liquid film by capillary pressure, but the spreading direction can be specifically defined. When the asymmetric surface is placed at an angle or vertically, liquid can slide in the one direction and get pinned in the other direction [13]. In summary asymmetric micro/nanostructured surfaces can improve surface performance, at the same time achieve surface directionality to bring extra functionality.

### 1.3 Dynamically Tunable Surfaces

While significant efforts have focused on fabricating various static micro and nanostructures with asymmetric features [9] [10] [11], which promises new opportunities in phase change heat transfer, microfluidic and other applications, the tunability has remained static and directly dependent on fabrication. On the other hand, dynamically tunable structures can greatly extend manipulation capability in these systems[15][16][17]. For example, pH/temperature-sensitive hydrogels that contract or swell in response to a stimulus were used to deform microstructures, and served as an ‘on/off’ switch for chemical reactions [16]. However this approach is limited because hydrogels require a liquid environment for actuation and cannot be applied to dry systems. Another method that has been pursued by many researchers in microfluidics is electrowetting, which use an electric field to modify surface wettability and tune fluid motion. It has been shown that when a voltage was applied to a liquid resting on the surface, the contact angle of a droplet showed dependence on the frequency of the applied voltage [18]. Hun *et al.* demonstrated that applying a voltage across fluid channel can attract fluid and switch its path [19]. However, it is difficult to mechanically tune the microstructures on a surface by electric field. Electrowetting also requires that the liquid to be in contact with electrode, restricting its application.

Due to these limitations of electrically tunable surfaces specifically for fluid applications, there has been increasing interest in magnetically tunable surfaces, where the magnetic micro/nanostructures on the surface can be mechanically controlled by an external magnetic field. Magnetics are also attractive due to the non-intrusive nature of magnetic fields. For example, PDMS micropillars containing cobalt nanowires have been used to apply forces to living cells, leading to different cellular reactions [17]. However with the low loading of magnetic particles in the polymer matrix, the magnetic strength was low, leading to a very small tilt angle. The random mixing of magnetic nanowires with PDMS also generated highly non-uniform deflection. For example, magnetic nanostructured surfaces with random geometries have been demonstrated to tune droplet contact angles [15]. Studies have also shown millimeter scale magnetic films which can deform to respond to external field [20]. However, fabrication of magnetic tunable surfaces with well controlled geometries and uniform deflection is very challenging. So far, uniform aligned arrays that can be dynamically tuned have not been demonstrated yet. We are interested in such surfaces with well-defined geometries and well-



controlled tunability as an experimental platform to study its impact on heat transfer performance, as well as optical, microfluidic and biological applications. Figure 2 shows concept of such surface and its potential applications.

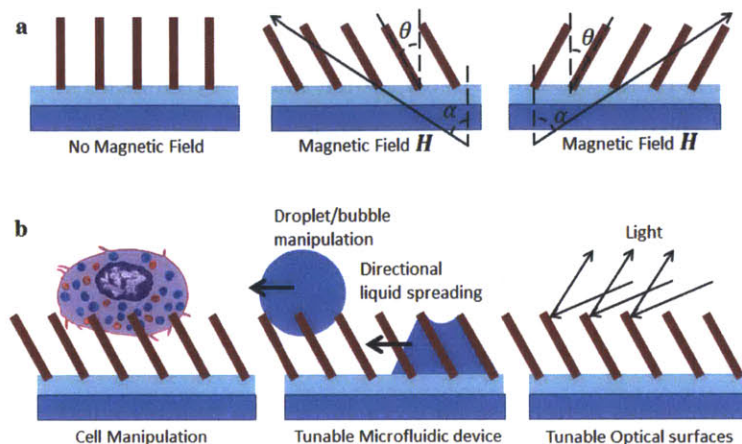


**Figure 2** Schematics showing a, The concept of magnetically tunable micropillar arrays where the tilt angle can be controlled via an external magnetic field and b, Various potential applications including cell, microfluidic, and light manipulation.

In this work, we present a novel fabrication process for the development of magnetically tunable uniform micropillar arrays, where the tilt angle and direction can be controlled upon application of an external magnetic field. Furthermore, this fabrication approach is easily repeatable and scalable to large areas with uniform pillar arrays greater than  $1 \text{ cm}^2$ .

Chapter 2 in this thesis describes and compares three designs for the magnetically tunable surfaces, among which design 3 appears most promising to realize fabrication and tunability. The fabrication of design 3 is then developed in detail. Chapter 3 shows characterization of the magnetization response of the electroplated nickel, and testing of tilt angles in a magnetic field. Chapter 4 presents modeling of the deflection angle. Finite element software (Abaqus) was used to acquire mechanical deformation of the PDMS layer when a torque was exerted on each of the pillar, and magnetic torque for each pillar in a magnetic field was calculated. Equilibrium was obtained when the magnetic torque generated by the field was equal to mechanical torque required to bend the structure. The measured tilt angle was in reasonable range of predicted value and the errors were discussed. Chapter 5 discusses interactions of the fabricated surfaces with water droplets, as well as future direction for improved surface tunability and a testing/control stage.



## 2. Design of Magnetically Tunable Surfaces

To realize tunable functions, three criteria are required to design well controlled arrays with dynamic magnetic tunability. First, the microstructures need to have strong magnetic material response, *i.e.*, a large magnetic torque must be generated to bend or deflect the microstructures. This criterion requires our choice of materials to have a high saturation magnetization. Strong permanent magnetic materials are the most ideal choices. However the actual design of material should also depend on fabrication feasibility and chemical compatibility for the real device.

Second, the surface must be structurally flexible, *i.e.*, it must be soft enough to easily deflect. This requires the material to have low Young's modulus. Also the deflection has to be elastic, in order for the material to restore to its original state.

Third, the geometry of the microstructures should be designed properly to: 1) allow mechanical flexibility, 2) provide the capability of large magnetic torque, and 3) satisfy the requirement of specific applications.

This chapter will discuss the criteria for the development of well controlled magnetic tunable surfaces. Based on the criteria, three design ideas of the magnetically tunable surfaces are presented and compared. Preliminary fabrication to prove the concept in each design is done and tested. Design 3 which electroplate magnetic pillar arrays and transfers the structure to a soft PDMS layer is the most promising design and thus is studied and developed. The fabrication detail is described in section 2.2.

### 2.1 Surface Designs

Based on the two criteria mentioned above, three approaches to designing magnetically tunable surfaces are discussed here.

#### ***Design 1: Embed Magnetic Particles into Cellulose Nanofibrils Templates***

This design combines a flexible template as mechanical support and magnetic nanoparticles as the source of magnetic torque. We used bacteria cellulose nanofibrils as flexible templates due to its large area to volume ratio and excellent mechanical flexibility. Cobalt ferrite nanoparticles were grown on the cellulose templates to magnetize the material [21]. Finally the

flexible and magnetic material was designed to be shaped into micro pillar arrays to define the microstructure geometry. Figure 3 shows the fabrication process and design.

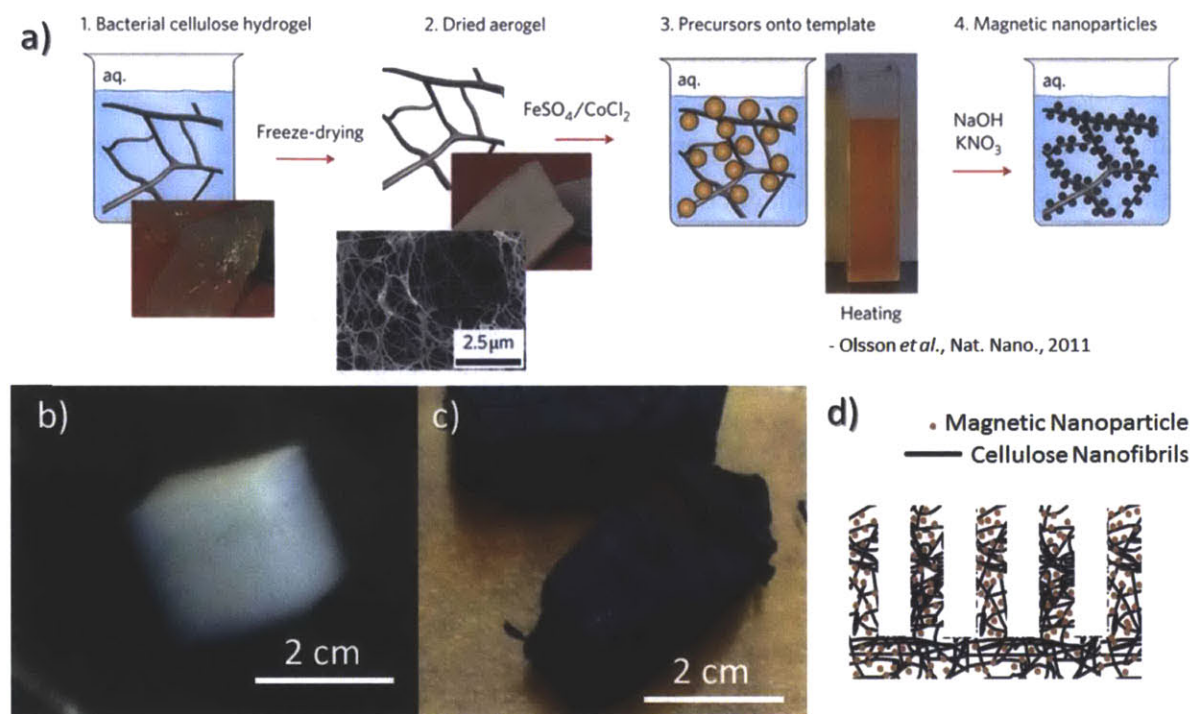


**Figure 3** Design and fabrication of cellulose nanofibrils embedded with cobalt ferrite magnetic nanoparticles. a, Material fabrication process, picture reproduced from [21]. b, Commercial available cellulose aerogel. c, Dry aerogel embedded with magnetic nanoparticles. d, Schematic design of the tunable surface.

The fabrication process for the magnetic porous material is as follows:

(1) Material: The bacterial cellulose hydrogel was produced by the bacterial strain *Acetobacter xylinum* FF-88. In our experiment commercially available bacteria cellulose hydrogel (Chaokoh coconut gel in syrup, Thep Padung Porn Coconut Co.) was purchased as shown in Figure 3b.

(2) The hydrogel ( $1\text{ cm} \times 1\text{ cm} \times 1\text{ cm}$ ) was rinsed with deionized water (DI water), followed by immersed in DI water for 3 hours to dilute sugar and other impurities concentration inside the hydrogel. It was then boiled in 10% sodium hydroxide (11.1 g/100 mL, approximately  $95\text{ }^{\circ}\text{C}$ ) for 3 hours and rinsed with DI water at room temperature for 6 hours to further purify the hydrogel.

(3) The hydrogel was immersed in a solution with 0.1, 0.165 or 0.2 mol/dm<sup>3</sup> total concentrations of FeSO<sub>4</sub>/CoCl<sub>2</sub> salts ([Fe]/[Co] = 2) for 1 hour to allow for diffusion of the solution into the aerogel. The system was then heated to 90 °C with stir agitation for 3 hours to initiate transformation of soluble iron/cobalt hydroxides into insoluble iron/cobalt oxyhydroxide complexes [21].

(4) KNO<sub>3</sub> was subsequently added to the solution until [Fe<sup>2+</sup>]/[NO<sub>3</sub><sup>-</sup>] = 0.44 while maintaining the temperature at 90 °C, and the system was kept at 90 °C for 6 hours to complete reaction and forming magnetic nanoparticles [21].

(5) The bacterial cellulose hydrogel embedded with magnetic nanoparticles was rinsed with DI water. Subsequently it was rapidly frozen by immersing in liquid nitrogen for 15 seconds. The frozen hydrogel was freeze dried for 12 hours in a vacuum chamber which is immersed in ice water environment. Other drying methods would destroy the porous cellulose structure due to surface tension of liquid while evaporating. After freeze-drying, the porous cellulose structure embedded with magnetic nanoparticles was preserved in a dry state. Figure 3c shows the fabricated flexible magnetic material.

Three different kinds of samples (C1, C2 and C3) were fabricated and their properties can be described from Table 1 in [21]. Assuming we could micromachine the fabricated material into micropillar arrays, our calculation (Figure 4) shows deflection angle of maximum 30° of sample C3 (aspect ratio = 3) can be achieved at field strength of 1 tesla and field angle of 60°, showing the fabricated material is very promising for fabrication of magnetically tunable micropillar arrays. Detailed calculation is described in Appendix.

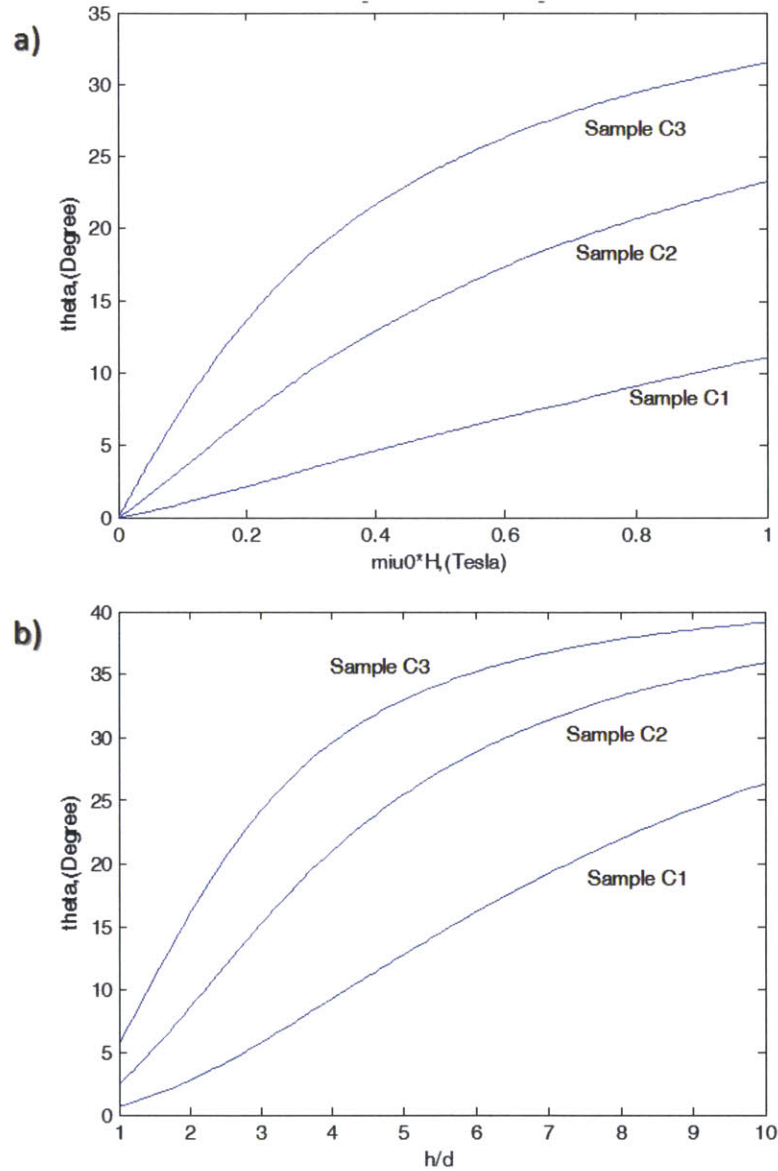


**Figure 4** Deflection angle as a function of external magnetic field and aspect ratio. a, Deflection angle vs. external magnetic field when  $h/d = 3$ . b, Deflection angle vs.  $h/d$  when external magnetic field is 0.5 tesla. Field angle is  $60^\circ$ .

While the material showed excellent mechanical flexibility and strong response to magnetic field, however, it was extremely difficult to machine the material into micropillar structures. One method was to press the material into a microhole array mold. However due to the intertwining nature of the nanofibril networks, molding the material into microstructures within the elastic regime was difficult to realize. An alternative was to cultivate the bacteria *Acetobacter xylinum* FF-88 which would produce the desired cellulose fibrils inside the mold, forming cellulose micropillar arrays structure first, then magnetize the structured surface by the

embedding magnetic nanoparticles into the material. However the aerobic bacterial strain *Acetobacter xylinum* FF-88 did not produce high density cellulose in a relatively low-oxygen level environment inside the microhole space in the mold. In summary, although this design utilizes a flexible and magnetic material, machining the material into the desired structure is challenging.

### ***Design 2: Machining Composite Magnetic Material into Micropillar Arrays***

This design overcomes the difficulty of molding complex cellulose networks by molding the template first, and then magnetizing the material by adding nano magnetic particles. The fabrication process is described below:

(1) The mold in this design was made by laser cutting acrylic board (2.5 mm) to form arrays of through-holes on the board.

(2) Suspensions of cobalt ferrite particles in water with a high concentration of sodium hydroxide were synthesized using the same method as described in Design 1 (step 3 and step 4, solution without bacterial cellulose hydrogel). The suspension was diluted by DI water. When the magnetic particles were precipitated to the bottom of the solution, the clear sodium hydroxide solution was taken away by pipet. The step is repeated a few times until pH of the suspension is below 8.

(3) We prepared a cross-linkable polymer solution which contains 66 wt% poly(ethylene glycol) diacrylate (PEG-DA,  $n=400$ ), 3.0 wt% 2-hydroxy-4-(2-hydroxyethoxy)-2-methylpropiophenone as photoinitiator, 30 wt% phosphate-buffered saline (PBS), and 1 wt% surfactant (Tween-20) [22]. After that, the concentrated suspended magnetic particles were added into uncross-linked polymer solution at liquid state and mixed well. The mixture was poured onto the acrylic mold, and was exposed under UV light until the polymer was cross-linked, forming PEG hydrogel.

Figure 5 shows the cross-linked hydrogel without magnetic particles and the composite cross-linked hydrogel with magnetic particles.



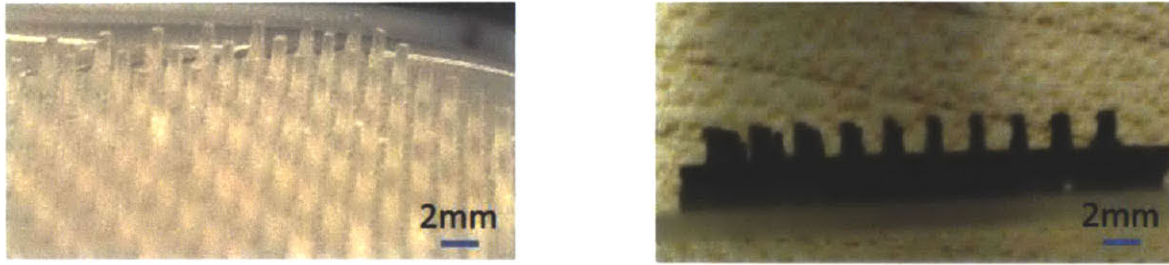


**Figure 5** Magnetic microstructured surfaces fabricated with composite materials. a, Hydrogel structure without magnetic particles. b, Hydrogel structure with magnetic particles.

Although magnetic structured surfaces could be fabricated by this method, it was limited in two ways: poor mechanical property and low material magnetic response. The as-fabricated micropillar arrays appeared brittle under a bending force, and tended to break when the deflection angle reached approximately  $30^\circ$ . More importantly due to the UVcuring nature of the hydrogel, concentration of cobalt ferrite magnetic nanoparticles was kept low in order for UV light to go into the material. When concentration of magnetic particles was high which made the composite material highly opaque, only the surface of the polymer could be cross-linked while UV light could not access beneath the surface to promote a cross-link reaction. Due to this limitation of the magnetic particle concentration, the composite material's magnetization was low, indicating it could not generate enough magnetic torque to deflect the pillar arrays. In conclusion, design 2 followed the design guidelines of combining magnetic material with moldable substrate, however it was challenging to realize surface tunability due to low magnetization.

### ***Design 3: Electroplating Magnetic Pillars Attached to Soft Substrate***

Design 3 overcomes the main limitations in design 1 and 2, which were poor moldability, low magnetic response and high stiffness of substrate. This design achieved high material magnetization by maximizing magnetic material volume. In this case, the micropillars were completely made of magnetic material by electro-deposition. The substrate supporting the magnetic micropillar arrays was polydimethylsiloxane (PDMS), which has a Young's modulus of only 360-870 kPa [23]. Figure 6 shows the design mechanism. Since this design could provide both high magnetic material response as well as mechanical flexibility, we developed the magnetic tunable surface based on this design.

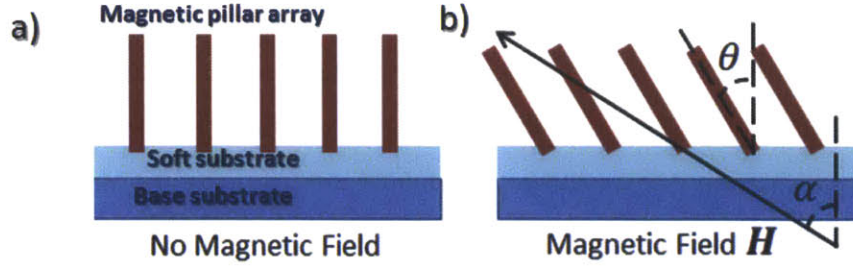


**Figure 6** Schematic showing mechanism of design 3. a, Magnetic pillar array fabricated by electroplating, transferred to soft substrate, supported by base substrate. b, When a tilted external magnetic field is applied at an angle  $\alpha$ , the magnetic pillar arrays respond to the field to a tilt angle of  $\theta$ .

## 2.2 Fabrication to Realize Tunable Surfaces

The tunable surfaces consist of ferromagnetic micropillars with diameters of 24-27  $\mu\text{m}$ , heights of 60-80  $\mu\text{m}$ , and spacings of 60  $\mu\text{m}$  resting on a soft PDMS substrate to achieve high tilt angles. The magnetic pillar arrays were fabricated by electroplating nickel, then bonding to PDMS surface by a silica adhesion layer. Figure 7 summarizes the fabrication process and the details are described as follows.

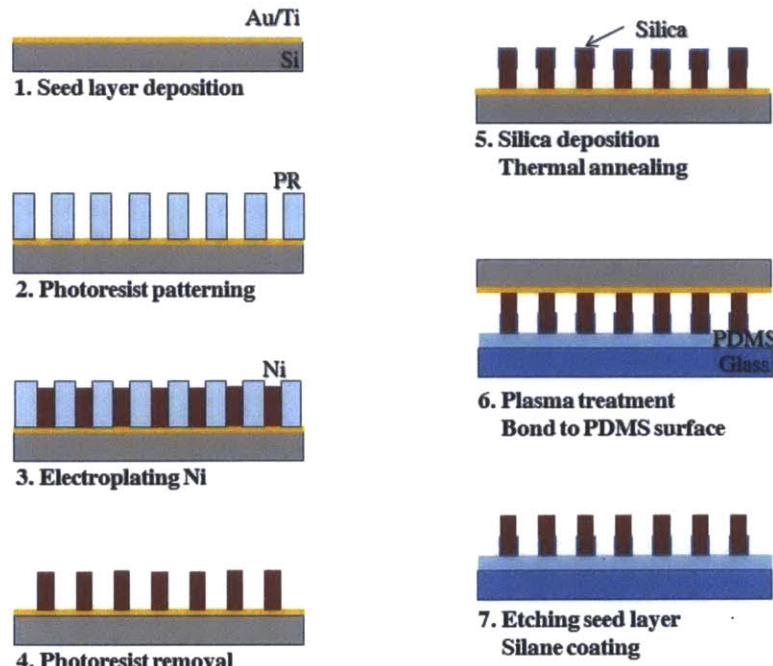


**Figure 7** Fabrication process flow for magnetically tunable micropillar arrays with controlled geometry.

(1) Seed layer deposition: After piranha clean of a 6-inch silicon wafer (S64600, WaferNet, Inc), a 20 nm titanium (Ti) was first deposited on the silicon substrate by e-beam thermal evaporation as adhesion layer, on top of which a 100 nm gold (Au) was deposited as the main seed layer. Gold was chosen because its chemical inertness could prevent side reactions in the following steps.

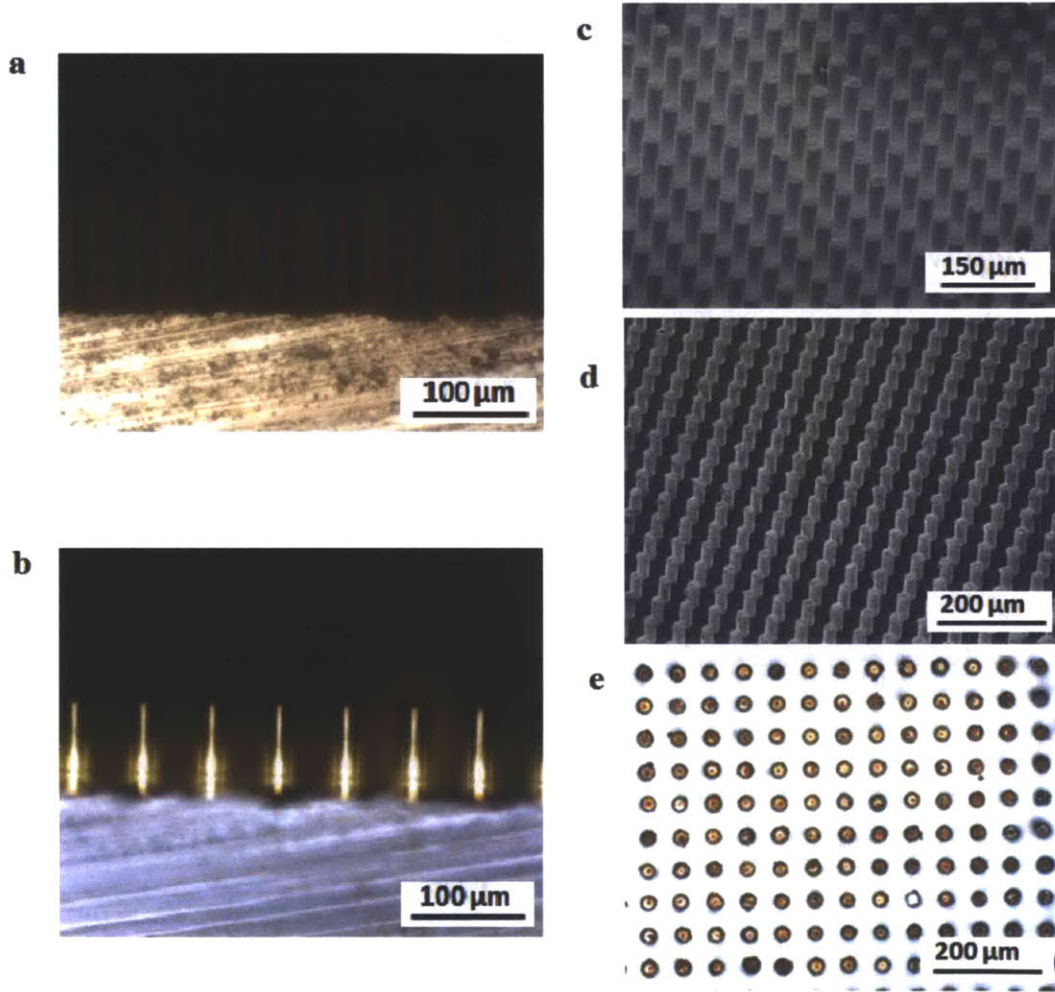


**Figure 8** SEMs of fabricated tunable micropillars with diameters of 24-27  $\mu\text{m}$ , heights of 60-80  $\mu\text{m}$ , and spacings of 60  $\mu\text{m}$ . Optical microscope images of a sample after a, step 2 and b, step 4. SEMs after c, step 4 and d, step 7. e, Optical microscope image (top down view) of a sample after step 7.

(2) Photoresist patterning: A 100  $\mu\text{m}$  thick negative photoresist (KMPR 1050, MicroChem) layer was spin-coated on the seed layer at 1300 rpm for 30 s, soft baked on a hotplate at 100  $^{\circ}\text{C}$  for 27 min, exposed to UV illumination at 750  $\text{mJ}/\text{cm}^2$ , post baked at 100  $^{\circ}\text{C}$  for 6 min and developed inside a sonication bath for 15 min to expose the seed layer in the



patterned region (Figure 8a). The result was a thick photoresist layer with uniform hole arrays. The wafer was then diced into  $2 \times 2 \text{ cm}^2$  samples.

It should be noted that for a photoresist layer as thick as 100 microns, the UV exposure dose has to be precisely adjusted to produce a vertical side wall (Figure 8a). A slanted sidewall, if the result is a smaller bottom and larger top opening, when photoresist layer is stripped, the electrodeposited metal will detach from the seed surface as well. In this sense, any over exposure, as well as underdevelopment, should be avoided (Figure 9b).

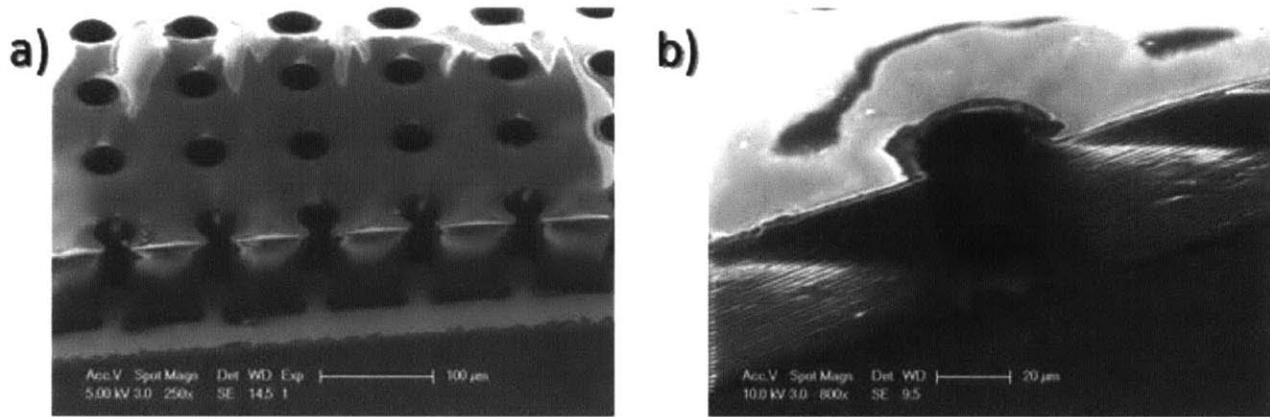


**Figure 9** SEMs of photoresist mold on Au seed layer. a, Fully open bottom Au surface. b, Photoresist residue on the bottom Au surface.

(3) Electroplating nickel: To enhance the hydrophilicity of the photoresist mold surface, the sample was treated with oxygen plasma at 29 W/500 mTorr/30 min. The contact angle of the commercial nickel electroplating solution (Nickel Sulfamate RTU, Technic Inc) on the photoresist patterned surface was reduced from  $80^\circ$  to  $10^\circ$  after the treatment, which allowed easy escape of bubbles produced inside the mold during electroplating. The sample was first sonicated in plating solution for 45 sec to remove air trapped in the microhole arrays of photoresist. The system was transferred to a desiccator, at the same time a vacuum environment was created by connecting the desiccator to a pump. This step allowed further degassing of the microhole arrays, which guaranteed complete contact of exposed Au seed layer with the Ni plating solution.

A dense array of nickel pillars was subsequently obtained by electroplating [24]. Figure 10b shows the electroplating system. The plating bath was maintained at  $50 \pm 2^\circ \text{C}$  on a hotplate, with stirring speed of 60 rpm/min. The degased sample ( $2 \times 2 \text{ cm}$ ) was connected to an alligator as the cathode in the electroplating process, providing electrons for the nickel ions to

become nickel metal and deposit on the gold seed layer. A thin nickel/iron alloy plate (2×2 cm) was used as the anode, while the metal loses electron and form ions into the solution.

An electrical current was applied by a DC power supply under the constant current mode. In the first hour, current (1st hour current in Table 1) was kept at 2 mA/cm<sup>2</sup> to form a thin and uniform layer of Ni on the exposed Au surface. After that, current (regular current in Table 1) was increased to 12.5~13.5 mA/cm<sup>2</sup> to increase the nickel deposition rate to approximately 11.5 microns/hour. Three different samples were fabricated and the parameters used in electroplating were given in Table 1. Electroplating duration was controlled to achieve a final thickness of deposited metal of 60 μm to 80 μm.

**Table 1** Sample specifications and Electroplating parameters

Sample 2×2cm <sup>2</sup>	Diameter (μm)	Pitch (μm)	Metal area* (cm <sup>2</sup> )	1 <sup>st</sup> hour Current (mA)	Regular Current (after 1 <sup>st</sup> h) (mA)	Regular deposition rate (μm/h)	Regular electroplating duration (h)
A	26	60	0.636	1.0	7.3	11.5	6.5
B	32	65	0.715	1.2	8.2	11.5	6.5
C	36	70	0.831	1.5	8.8	11.3	6.5

\* When plating, only part of sample is immersed in plating solution, to prevent contact between alligator and plating solution, as shown in Figure 10b. We assume 85% area of sample is immersed in plating solution to calculate metal area.

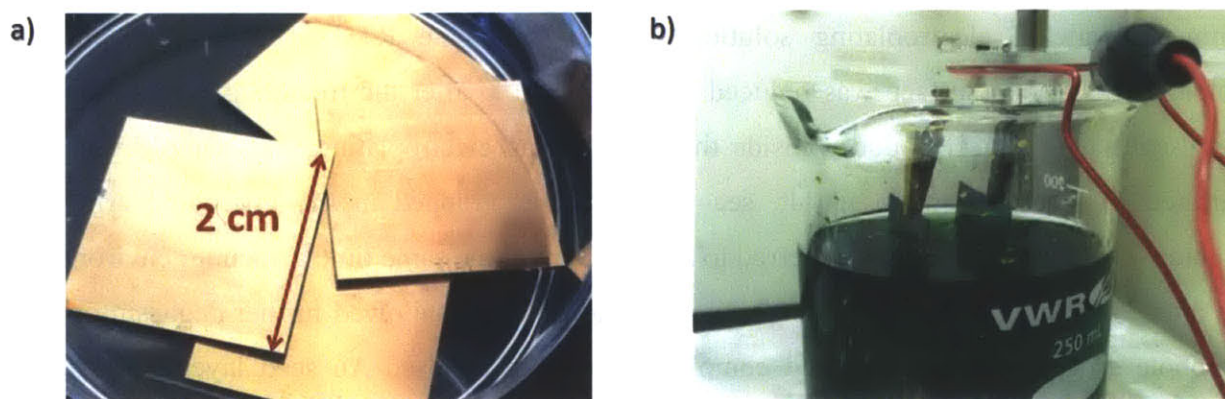


**Figure 10** Samples and electroplating setup. a, 2×2 cm samples for electroplating. b, Electroplating setup, with samples on the cathode and a nickel thin plate on the anode.

(4) Photoresist removal: To prevent detachment of the nickel pillars from substrate (Figure 11), the patterned photoresist layer was first softened and then lifted by immersing in acetone (room temperature, 8 hours) and in MicroChem Remover PG with stir (70 °C, 2 hours).

Photoresist residue was oxidized by sodium permanganate in an alkaline solution (XP Remover K) and dissolved in methane sulfonic acid (XP Neutralizer K), leaving freestanding pillars on the substrate (Figure 8b and 8c).

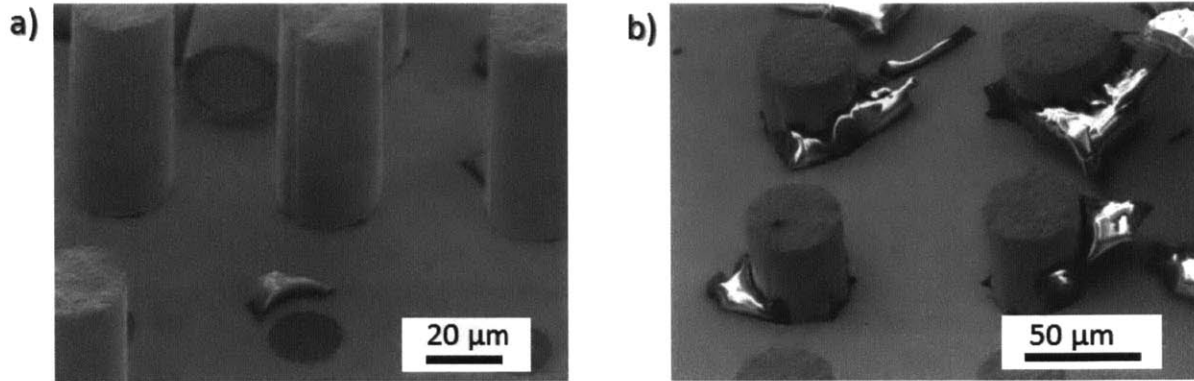


**Figure 11** Electroplated nickel. a, Detachment from seed layer. b, Photoresist residues.

(5) Silica deposition/thermal annealing: A 10 nm silica layer was deposited on the pillar tips by plasma-enhanced chemical vapor deposition (PECVD). The silica layer served as an adhesion layer between nickel pillars and PDMS substrate. To enhance magnetic performance, nickel pillars were annealed at 300 °C under vacuum with an applied magnetic field of ~0.5 tesla, perpendicular to the sample surface. The annealing step was optional since magnetization enhancement of nickel from thermal annealing was not significant.

(6) Transferring to PDMS: A 70 μm PDMS layer was spin-coated on a glass substrate, cured, and oxygen plasma treated (29 W/500 mTorr/10 min). The nickel pillars coated with silica on the tips were subjected to the same plasma treatment condition and bonded onto the PDMS surface. This transferring process has proven to be successful and robust.

Another transferring process which we have pursued but had difficulty was demonstrated in Figure 12. We first spin-coated a thin layer of PDMS on the nickel arrays as shown in Figure 12a following a method described in [25]. (The diluted solution was prepared by dissolving HMCTS (hexamethylcyclotrisiloxane, Alfa Aesar, 97% ) in methylene chloride, and add PDMS with hardener (10:1) to the solution. Keep the ratio to be HMCTS:PDMS = 3:1. Spin-cast on the nickel arrays at 2000 rpm for 2 min. The sample was cured at 150 °C for 30 min. The result was a thin film of PDMS on the seed layer) Then attach a kapton tape or diesaw tape (1044R-7.9 u.v release diesaw tape, Ultron System Inc) on the electroplated Ni arrays. The nickel arrays supported by PDMS were sheared off using a razor, then carefully transferred to a half cured



PDMS layer. The system was heated until the two PDMS layers adhered to each other. Releasing of the tape resulted in the final structure, as shown in Figure 12b. Although this transferring process was successfully demonstrated, it required extreme care. Figure 12c showed large area of defect happened during the transferring process.

Since the second transferring process had poor repeatability and feasibility, in the final design we used the first transferring method.

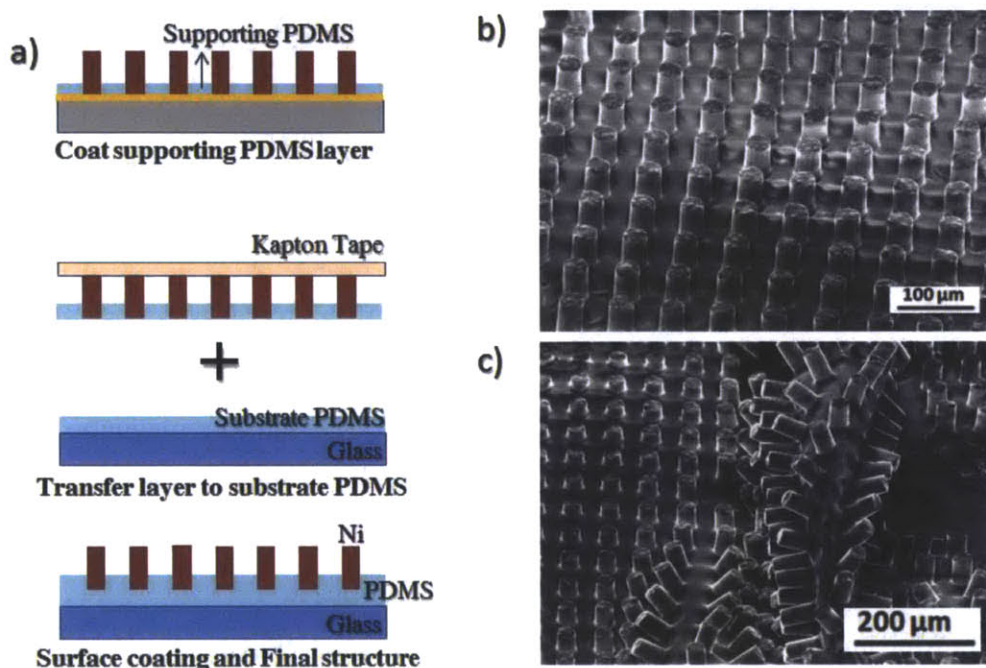


**Figure 12** Kapton tape aided transferring method. a, Process flow. b, SEM of a sample after transferring. c, SEM of a sample with defect area.

(7) Etching seed layer: The gold seed layer was etched away by gold etchant (Sigma-Aldrich) at 70 °C for 5 hours such that the pillars (detached from the silicon substrate) remained only on the PDMS substrate (Figure 8d and 8e).

In summary, this chapter described several approaches to fabricate magnetically tunable microstructured surfaces with well controlled geometries. Nickel micropillar arrays fabricated by electroplating onto patterned electrode were transferred and bonded to PDMS substrate as the final design. We successfully demonstrated fabrication of surfaces with uniform pillar arrays covering areas of 8 mm×8 mm as shown in the SEM (Figure 8d) and the top-down view with an optical microscope (Figure 8e). This fabrication process is easily repeatable and scalable to even larger arrays.

### 3. Characterizing and Testing

After surface design and fabrication discussed in Chapter 2, Chapter 3 focuses on sample characterization and surface tilt angle testing. Magnetization hysteresis loop of the plated Ni material was measured to verify magnetic response of a magnetic field. Magnetization reached saturation when the external field strength was approximately 0.3 tesla. We then tested tilt angle by placing the sample under optical microscope and moved a magnet under the sample to change field angle. The uniform tilt angle was found to be  $10.5 \pm 1^\circ$  when field strength was 0.5 tesla and maximum field angle was  $60^\circ$ .

#### 3.1 Characterizing Magnetization

After the photoresist removal (step 4 in Figure 8), we characterized the magnetic properties of the pillar arrays using vibrating sample magnetometry and confirmed that they match the properties of bulk nickel with a coercivity of 60 Oe and magnetization saturation at a field strength of 0.3 tesla, as shown in Figure 13.

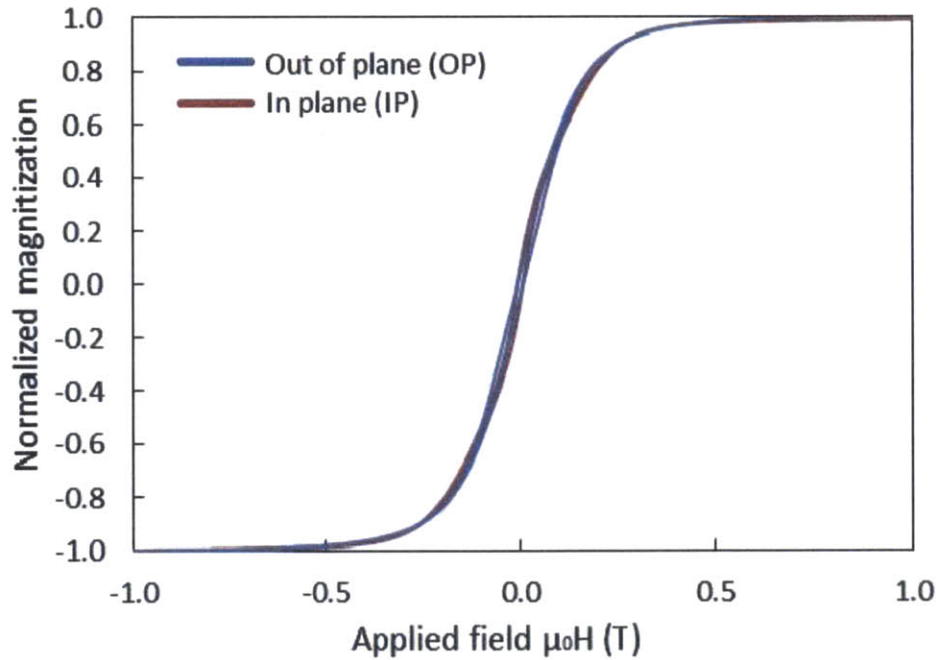


**Figure 13** In-plane and out-of-plane magnetic hysteresis loop of the electroplated nickel pillar arrays on a silicon substrate.

The small hysteresis indicates the magnetic softness of the electroplated nickel; even after annealing, the material could be easily magnetized to saturation in the field direction, as well as

de-magnetized after the field was removed. The magnetization direction of a soft magnetic material, however, depends on the constraints and applied field direction. The aspect ratio ( $\sim 2.5$ ) of the micropillars provided an easy-axis for the magnetization direction; under no constraints, the cylindrical nickel pillars were preferentially magnetized in its axial direction, and the pillars rotated to align with the field direction, while maintaining the axial magnetization direction. However, since the pillars were fixed on one end (standing on rigid silicon substrate), the magnetic microstructures were magnetized in the field direction regardless of its easy-axis direction, as indicated by the similarity of the measured hysteresis curves between the out-of-plane field direction and in-plane field direction (Figure 13). In the case of a partially constrained pillar array (sample after step 7, where pillars were constrained with one end on the soft PDMS substrate, but were allowed to tilt), when the pillars were first axially magnetized and subjected to changes in the field direction, the magnetization direction of the pillars followed the field direction, and decreased the angle between the magnetization of the pillars and the field. To generate a large magnetic torque to tilt the pillars, however, a large angle between the magnetization of the pillars and the field needs to be maintained. As a result, we realized dynamic tuning for our fabricated nickel microstructures by changing the field to keep a large angle between the magnetization of the pillars and the field.

### ***3.2 Tilt Angle Testing***

The fabricated surfaces were characterized under an optical microscope. A 5597 gauss axially magnetized neodymium disk magnet (D4H2, K&J Magnetics, Inc.) was first placed at a distance of 3 mm under the sample to introduce a magnetic field perpendicular to the sample surface. As a result, the micropillars were magnetized axially. After that, the disk magnet was moved horizontally and repeatedly at a frequency of around 30 Hz (Figure 14).



**Figure 14** Tilt angle testing setup. The tunable sample surface was fixed on a cover glass above the magnet.

Under these conditions, the maximum field strength and maximum field angle was estimated to be 0.5 tesla and  $60^\circ$ , respectively. Movement of pillar top surfaces was recorded using a camera (PixeLINK). Recorded images were analyzed to get the maximum tilt angle during pillar movement. The micropillars tilted uniformly with an average tilt angle of  $10.5 \pm 1^\circ$  (Figure 15a, side view and Figure 15b, top view). Measurement from both side view and top view showed consistent tilt angle.

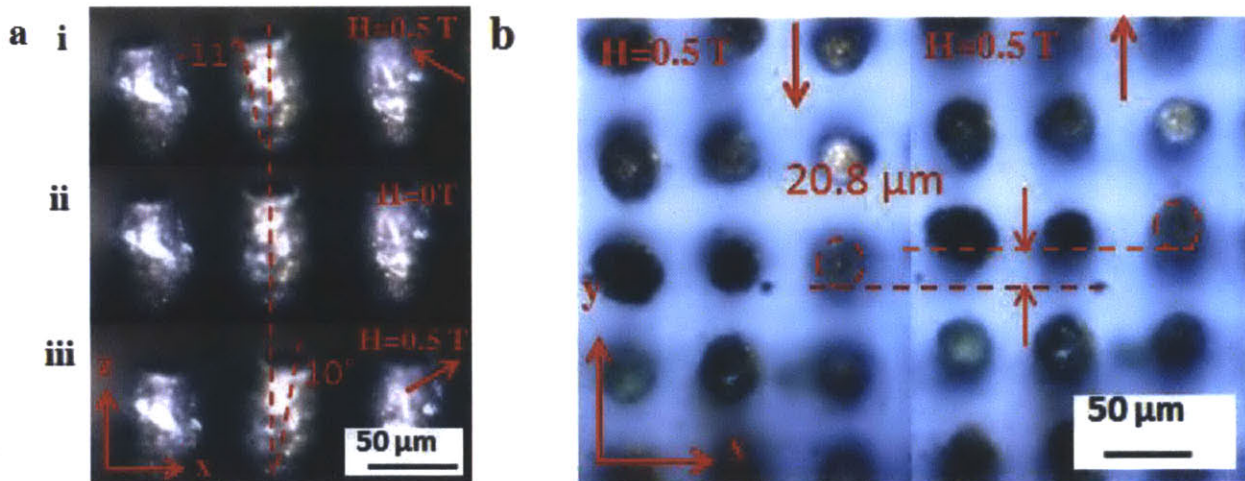


**Figure 15** Experimental demonstration of tilted pillars. a, Side view images of a tunable surface with a field strength of  $\sim 0.5$  tesla and field angle varied from  $-60^\circ$  to  $60^\circ$ . b, Top view images of a sample with a field strength of  $\sim 0.5$  tesla and field angle varied from  $-60^\circ$  to  $60^\circ$ .

In summary, magnetic properties of the pillar arrays was characterized using vibrating sample magnetometry and the result showed a small coercivity. Magnetization saturated quickly with an external magnetic field of 0.3 tesla. Tilt angle was measured under an optical microscope. Both side view images and top view images were recorded by pixeLINK camera. The measurement from both side view and top view images showed a consistent and uniform  $10.5\pm1^\circ$  tilt angle. By far we have demonstrated dynamically tunable micropillar arrays with well controlled geometry and uniform tilt angles.



## 4. Simulation and Modeling

### 4.1 Mechanical Deflection Simulation

With the fabricated pillar geometry and magnetic properties, as well as the experimental configuration, we performed finite element simulations using Abaqus to determine the equilibrium position of the pillars under different mechanical torques  $T_{\text{mech}}$ . The model consists of nickel pillars (80  $\mu\text{m}$  in height and 26  $\mu\text{m}$  in diameter) with 20  $\mu\text{m}$  of one ends embedded into a layer of 100  $\mu\text{m}$  soft PDMS.

A dynamic model depicting a unit cell was built first to simulate the deformation of the PDMS layer (Figure 16). A single cylindrical nickel pillar (80  $\mu\text{m}$  in height and 26  $\mu\text{m}$  in diameter) was built, with 20  $\mu\text{m}$  bottom end embedded in a 60  $\mu\text{m} \times 60 \mu\text{m}$  (pitch length)  $\times$  100  $\mu\text{m}$  PDMS block. Boundary conditions were: 1) the bottom surface of the PDMS layer was fixed; 2) the contact surface between PDMS and pillar bottoms were tied together; 3) other surfaces of PDMS and pillars were free surfaces. The free sidewall surfaces of PDMS, however, did not capture the periodic boundary condition. In the real system the front and back PDMS surface should have the same displacement. This non-ideality was considered in the next model. For simplified first-step estimation, the free surface boundary condition was kept. Hexahedron meshes whose sizes were around 1 micron were created, while finer meshes were developed at the contact surfaces between PDMS and nickel pillars where the strain was the largest.

A dynamic load was applied to the pillar in the form of two forces: a +x direction force was applied on the top surface of cylindrical pillar and a -x direction force with the same magnitude was applied on the bottom surface. Since the Young's modulus of nickel is much larger than that of PDMS, the cylindrical nickel pillar acted almost like a rigid body. The result was a net torque  $T_{\text{mech}}$ ,

$$T_{\text{mech}} = F \times h \quad (1)$$

where  $T_{\text{mech}}$  is the mechanical torque,  $F$  is the force and  $h$  is the height of the pillar.

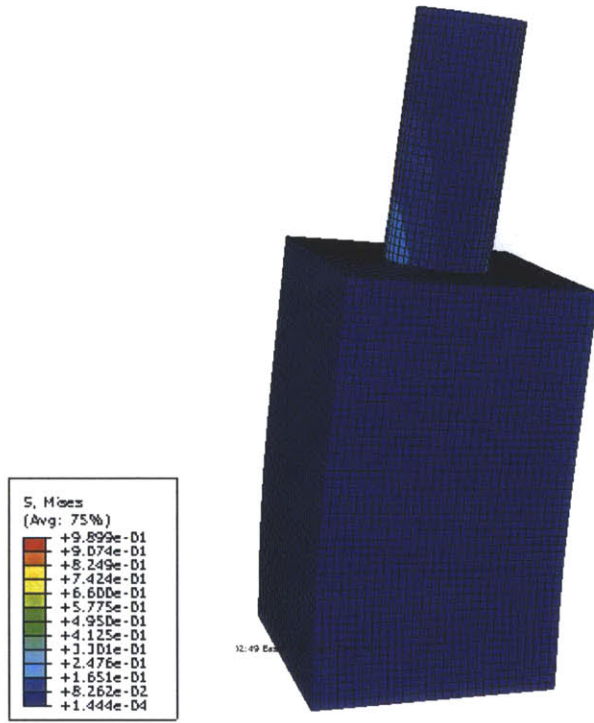


**Figure 16** Finite element simulation a unit cell with dynamic load of  $4 \times 10^{-10}$  Nm.  $h=80 \mu\text{m}$  (60  $\mu\text{m}$  above PDMS surface and 20  $\mu\text{m}$  embedded in PDMS) and  $d=26 \mu\text{m}$ . Predicted tilt angle was  $3.4^\circ$

Load was applied in a dynamic manner: at time  $t=0$  s both forces were 0 N. After a linear increase, the load reached prescribed value and remained constant at time  $t = 0.8$  s. Explicit method was used as an efficient way to calculate tilt angle. While the explicit method is computationally faster than implicit method, it sacrifices its accuracy and often results in vibration after equilibrium has been reached, as shown in Figure 17 where the systems reached equilibrium at time 1.7 s when the slope of the curve changed dramatically, and continued into the vibration stage.

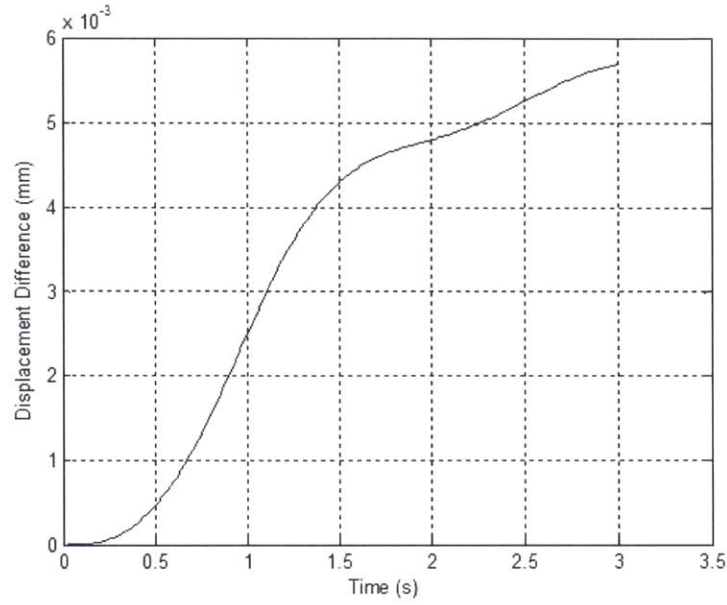


**Figure 17** Displacement difference in the x-direction between top pillar surface and bottom pillar surface as a function of time. A dynamic load of  $4 \times 10^{-10}$  Nm was applied.

To increase accuracy as well as to represent periodic boundary conditions, the implicit method was used and five pillars were considered in the revised model, where the deflection angle of the middle pillar was selected to represent the real case. Similar boundary conditions were applied here (as shown in Figure 18): 1) the bottom surface of the PDMS layer was fixed; 2) the contact surface between PDMS and pillar bottoms were tied together; 3) other surfaces of PDMS and pillars were free surfaces. We used hexahedron meshes whose sizes were around 1 micron. Finer meshes were created at the contact surfaces between PDMS and nickel pillars where the strain was the greatest. A mechanical torque was applied on each of the pillars in a clockwise direction.

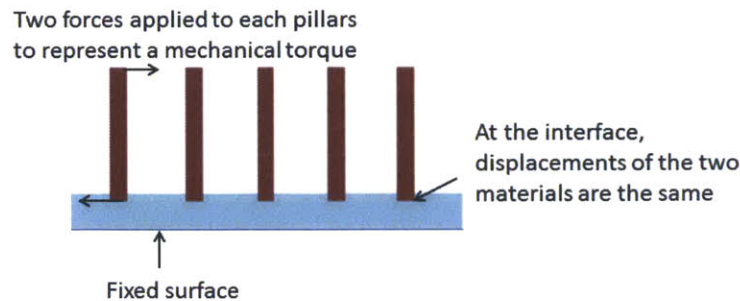


**Figure 18** Schematic of boundary conditions and load of the model. Bottom surface of PDMS is fixed, contact surfaces of PDMS and nickel pillars are tied together (same displacement). Other surfaces are free surfaces. A mechanical torque is applied to each of the pillars.

Two forces with the same magnitude, along +x direction and -x direction respectively, were exerted on the top and bottom surfaces of each of the pillars to represent a mechanical torque. Under each of the applied torques ranging from 0 Nm to  $3.2 \times 10^{-9}$  Nm, the implicit method was used to obtain equilibrium tilt angle (Figure 19). Further calculation when tilt angle exceeded  $12^\circ$  was not conducted both due to the linear behavior of the tilt angle curve and the excess amount of calculation time.

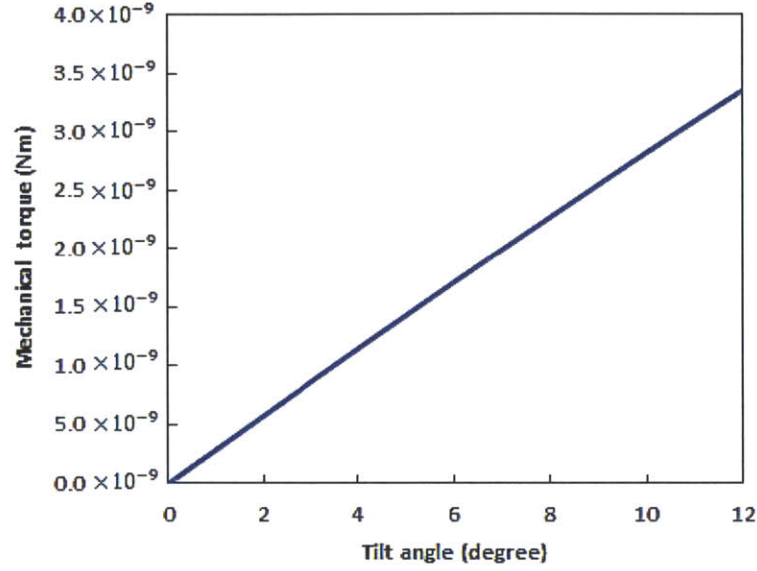


**Figure 19** Finite element (Abaqus) simulation of tilt angle as a function of mechanical torque when  $h=80 \mu\text{m}$  ( $60 \mu\text{m}$  above PDMS surface and  $20 \mu\text{m}$  embedded in PDMS) and  $d=26 \mu\text{m}$ .

Figure 20 is result of simulation tilt angle when a torque generated by 0.7 tesla field at  $60^\circ$  field angle is applied to each pillar. The tilt angle of middle pillar can represent the periodic boundary condition and is chosen for calculation. The largest strain (shown in red color) happened at the interface between pillar and PDMS substrate.

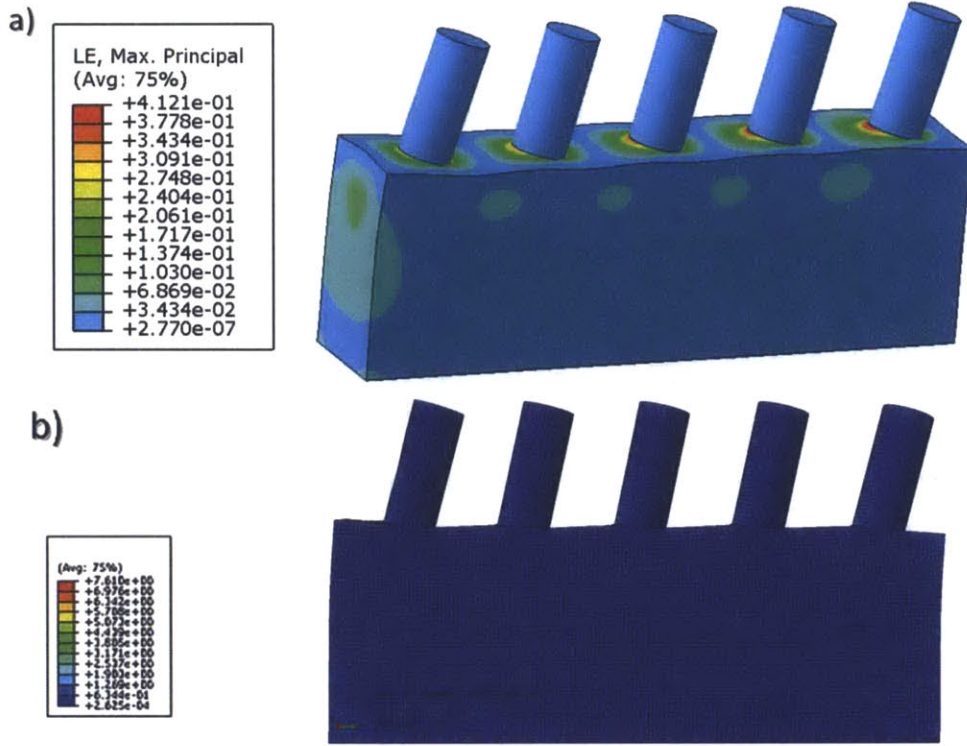


**Figure 20** Finite element simulation of tilt angle when  $h=80\text{ }\mu\text{m}$  ( $60\text{ }\mu\text{m}$  above PDMS surface and  $20\text{ }\mu\text{m}$  embedded in PDMS) and  $d=26\text{ }\mu\text{m}$  under a mechanical torque when the field strength was 0.7 tesla and field angle was  $60^\circ$ . The predicted tilt angle was  $20^\circ$ . a, 3D view. b, Side view with mesh shown.

## 4.2 Magnetic torque

In the previous section, we analyzed deflection angle as a function of an applied mechanical torque. However in the actual case, this torque is generated by a magnetic field. In this section, we investigated how much magnetic torque could be generated given a specific magnetic material, the material geometry and magnetic field.

Consider the case shown in Figure 21. A micropillar made of magnetic material placed inside a magnetic field, assuming axial direction of magnetization of the pillar. Pillar is at angle  $\theta$  with respect to a reference direction. The field is applied at angle  $\alpha$  with respect to the same reference direction.



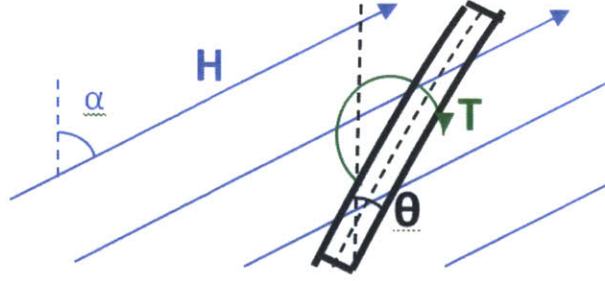


**Figure 21** A magnetic micropillar placed inside a magnetic field. Assuming axial direction of magnetization of the pillar. Pillar is at angle  $\theta$  with respect to a reference direction. Field is at angle  $\alpha$  with respect to the same reference direction.

Outside of the pillar, the magnetic flux density  $\vec{B}$  and magnetic field intensity  $\vec{H}$  obeys the equation (2),

$$\vec{B} = \mu_0 \vec{H} \quad (2)$$

where  $\mu_0$  is the vacuum permeability,  $\mu_0 = 4\pi \times 10^{-7}$  Henry/m

Due to magnetization, the magnetic flux density inside the pillar is

$$\vec{B} = \mu_0 (\vec{H} + \vec{M}) \quad (3)$$

where  $\vec{M}$  is the magnetization of cylindrical microstructures.

The magnetic torque was calculated by equation (4),

$$T_{\text{mag}} = V \vec{M} \times \vec{B} \quad (4)$$

where  $V$  is the volume of magnetic pillar,  $\vec{M}$  is the magnetization of cylindrical microstructures and is assumed to be in axial direction, and  $\vec{B}$  is the magnetic flux density.

Considering the pillar geometry, the volume can be described as,

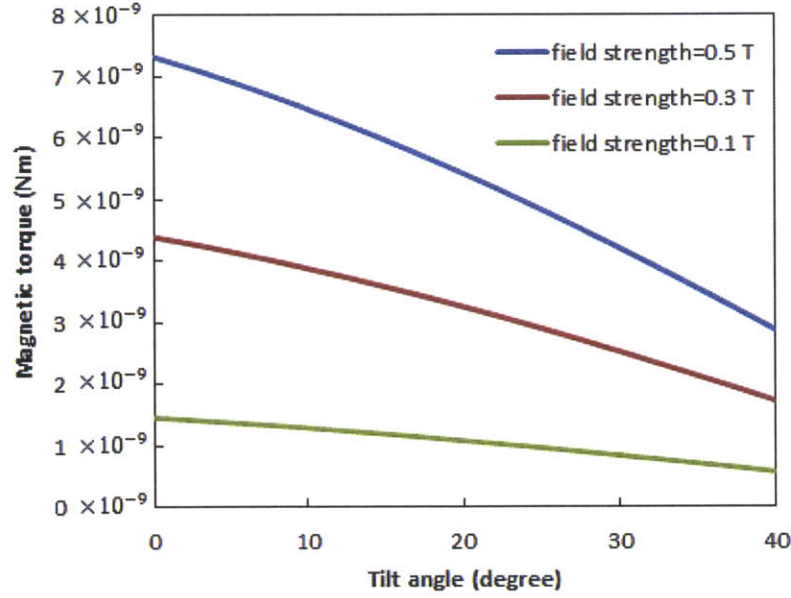
$$V = \frac{\pi}{4} d^2 h \quad (5)$$

where  $d$  and  $h$  are the diameter and height of pillars.

From equation (3), (4) and (5), can be rearranged into equation (6),

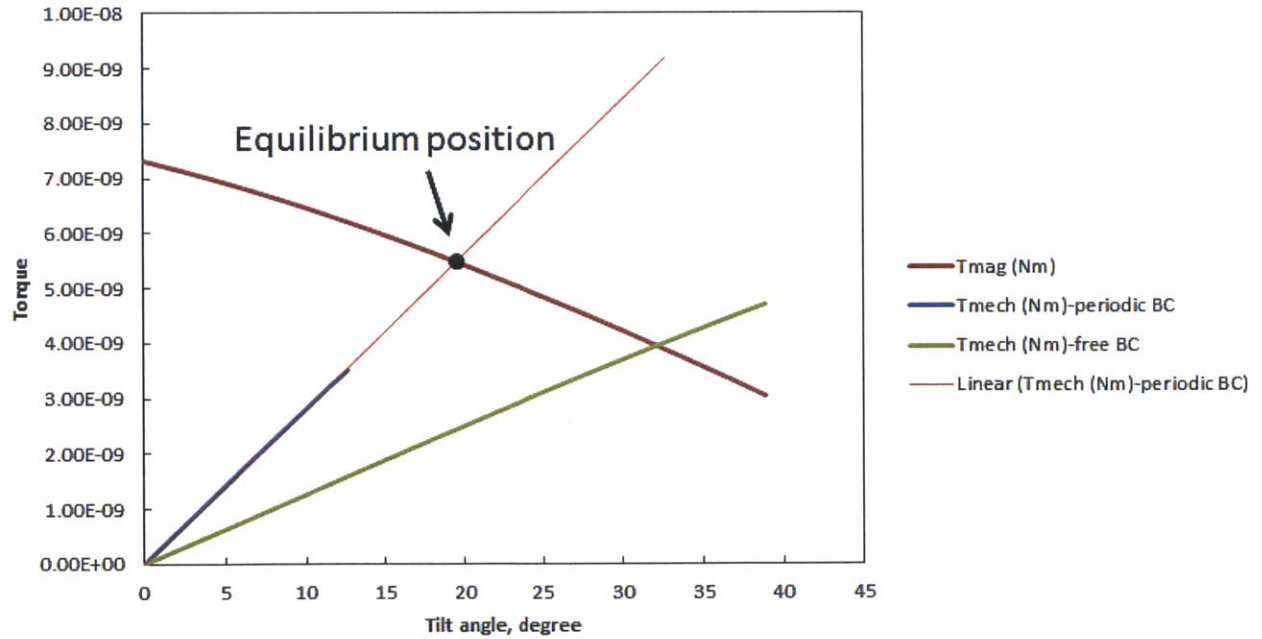
$$T_{\text{mag}} = \frac{\pi}{4} d^2 h M \mu_0 H \sin(\alpha - \theta) \quad (6)$$

where  $M$  is the magnitude of magnetization,  $\mu_0$  is the vacuum permeability,  $H$  is the magnitude of applied field,  $\alpha$  is field angle defined as the angle between applied field and surface vertical direction, and  $\theta$  is the pillar tilt angle.



**Figure 22** Calculation of magnetic torque as a function of tilt angle. Field angle was 60°.

At equilibrium, the magnetic torque exerted on a single pillar should equal the mechanical torque needed to tilt the pillar. As an example, a 20° tilt angle was predicted with a torque generated by a magnetic field strength of 0.7 tesla at a 60° angle (Figure 23).



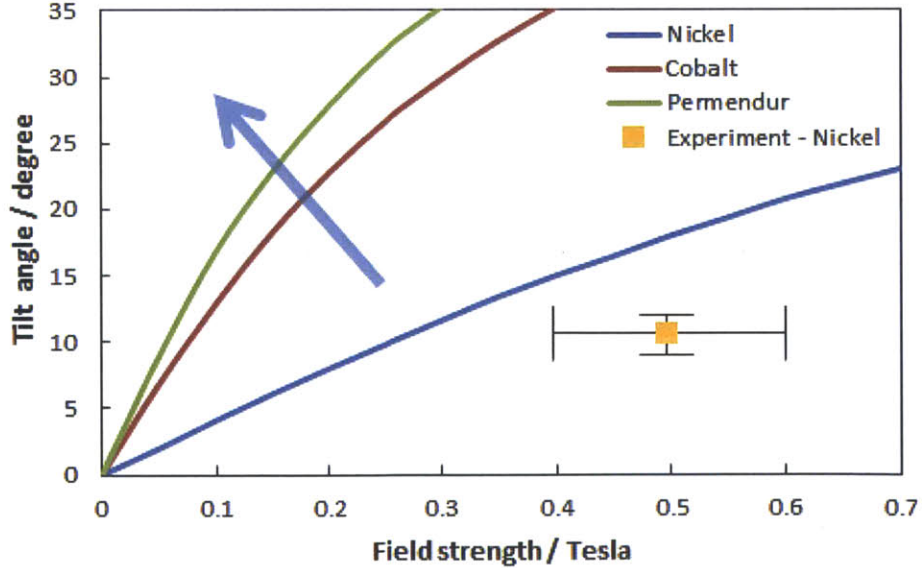
**Figure 23** Equilibrium point determined by the intersection of mechanical torque and magnetic torque.

Figure 23 shows the mechanical torque as well as the magnetic torque. The simulated mechanical torque with a periodic boundary condition (blue line) differed from the free boundary

condition (green line) simulated the mechanical torque almost by a ratio of two. Under the same torque, the periodic boundary condition which emulated the real scenario gave smaller deflection angles.

Since at equilibrium, the magnetic torque exerted on a single pillar should equal the mechanical torque needed to tilt the pillar, by combining the simulation results (Figure 19) with the magnetic torque calculation (Equation (6), or Figure 22), the equilibrium tilt angle was obtained (Figure 22). The black dot in Figure 23 represents the equilibrium point of a nickel pillar under a specific field condition (field strength is 0.6 tesla, field angle is  $60^\circ$ ).

The mechanical torque as a function of tilt angle is a fixed curve (blue line) and only depends on the geometry and material properties. Magnetic torque (Equation (6)), however depends on the field strength, field angle, and the magnetic micropillar material magnetization. We can plot magnetic torque curves under variant conditions with the same mechanical torque curve and look for the intersection equilibrium points. Figure 24 shows the result of the equilibrium tilt angle as a function of field strength when the field angle is kept at  $60^\circ$ .



**Figure 24** Simulation result of tilt angle as a function of field strength while field angle is kept at  $60^\circ$  with different magnetic materials. Square symbol shows experimental result with fabricated nickel pillars. The uncertainty in tilt angle was from multiple measurements and imaging processing, while the uncertainty in field strength was due to the inaccurate control of the magnet.

The experimental results (square symbol in figure 24) showed reasonable agreement with the model; however we attribute the discrepancy to the following factors:



- a) Uncertainty in the Young's modulus of the fabricated PDMS layer
- b) The field strength and angle at the sample surface
- c) The existence of a non-magnetic oxide layer on nickel pillars
- d) The magnetic softness of the nickel material

Understanding the discrepancy would provide insights as how to improve and optimize the tunable surfaces. Among the four factors, the rough estimation of field strength and angle may have the strongest impact to the uncertainty of the result. Clearly, a better testing stage is needed to test tilt angle as well as precisely providing a field for the real device.

Furthermore, while we demonstrated a reasonable tilt angle, we investigated the effect of different magnetic materials to broaden the applicability of this work. While saturation magnetization of bulk nickel is 0.6 T, saturation magnetization of cobalt is 1.7 T, almost three times larger than that of nickel. Figure 24 shows that by changing the magnetic material from nickel to cobalt or permendur (50% cobalt and 50% nickel), we can increase the tilt angle, meanwhile decrease the magnetic field strength significantly. These results suggest a promising future fabrication direction (arrow) for magnetically tunable arrays.



## 5. Discussions

### 5.1 Surface interaction with water droplets

To test the interaction of the tunable surfaces with fluid, we investigated two different wetting states: Cassie Baxter wetting state and Wenzel wetting state. We wanted to examine whether the tunable surface could control droplet directionality and motion. In both cases we coated the surface with silane (tridecafluoro-1,1,2,2, tetrahydrooctyl-trichlorosilane) to create a hydrophobic surface.

However, experiment to test the surface interaction with a fluid was not straight forward. Since the adhesion force of a  $\sim 10\ \mu\text{L}$  drop with a fluid injecting device (syringe or pipette) was larger than that of the droplet with the surface, it was difficult to initially place the droplet on the surface. The surface only attracted droplets from a pipette if there was a hydrophilic defect spot. In this condition, the droplet was pinned and thus unable to move.

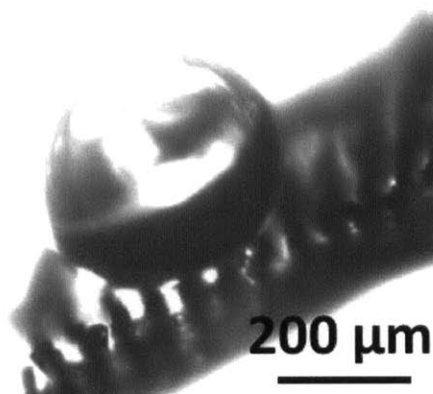


**Figure 25** Optical microscope image of a partially wetting liquid sitting on the fabricated magnetically tunable surfaces.

Attempts to deposit smaller droplets were also unsuccessful since droplets were in a partially wetting state rather than the Cassie Baxter state. We injected DI water droplets whose sizes were on the order of 100 nm at a frequency of around 1000 Hz. This continuous injection resulted in one accumulated droplet, as shown in Figure 25. Since the individual droplets injected was too small, the accumulated droplet always grew from a spot between the pillars while it grew to the top and started to spread on the pillar tips. Due to the partially wetting condition, the droplet was also pinned.

The droplet was highly pinned when it formed the Wenzel state. In this scenario we observed unexpected degradation of the surface microstructures as shown in Figure 26. When the droplets wet the surface, adhesion between the pillar arrays and the PDMS substrate weakened. When an external magnetic field at an angle was applied, we observed pillars detaching from PDMS surfaces and forming stacks. Although this phenomenon showed the rapid degradation of the surface, it also presents an opportunity for self-assembled magnetic pillar arrays, since the detached pillar can connect to their adjacent pillars. The connection was not a fixed bonding between the contact surfaces of two pillars, but was rather due to the magnetic attraction force. Therefore it does not require a large bending moment to tilt the micropillars and the tilt angle was much larger than that of the pillars bonded to the surfaces. This surface can be potentially useful for optical systems with tunable reflectance and transmittance, sensors or switches for chemical reactions, and cell manipulation which does not require a strong bending torque. However less bonding restriction at the interface also means weaker connection. The microstructures might easily detach and form surface defects, which limits its potential application in microfluidic systems where surface tension of fluid is dominant.

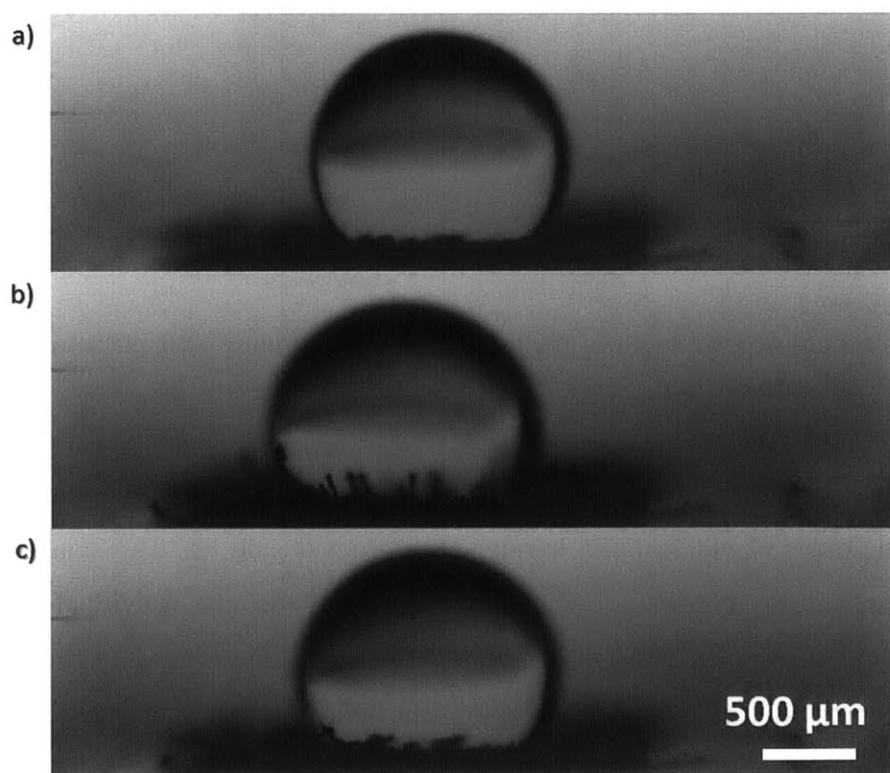


**Figure 26** Optical microscope images of a Wenzel state droplet and detachment of the nickel pillars. a, Without magnetic field. b, With a magnetic field perpendicular to the surface, pillars detached from surface were observed. c, With a magnetic field of 0.5 tesla. Field angle was 80°.

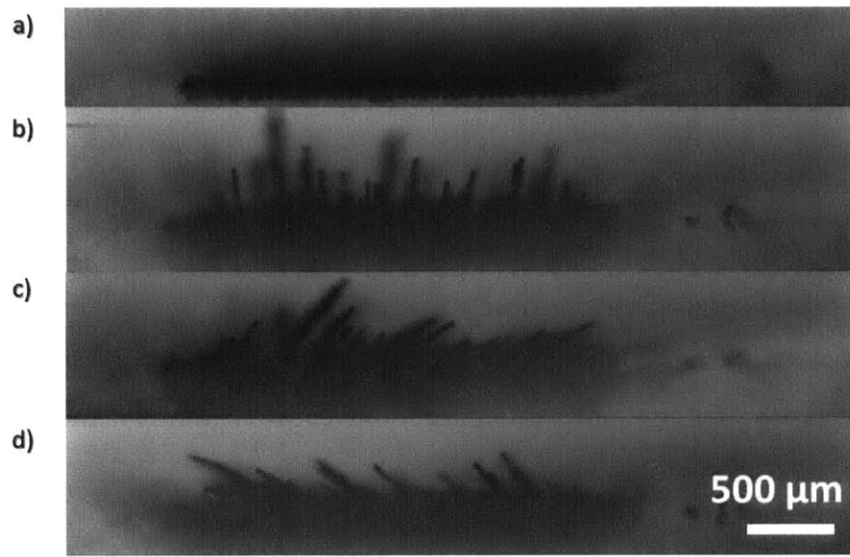


**Figure 27** Optical microscope images of a fabricated surface before wetting and after wetting. a, Without magnetic field and no detachment was observed. b, After wetting, detached pillars formed stacks. Magnetic field was 0.5 tesla, perpendicular to the sample. c, With a magnetic field of 0.5 tesla. Field angle was  $80^\circ$  to the right. d, With a magnetic field of 0.5 tesla. Field angle was  $80^\circ$  to the left.

## 5.2 Directions for the future

In this study we designed and developed a novel fabrication process for magnetically tunable microstructured surfaces. We successfully fabricated the tunable surfaces with repeatability and the surface could be scaled to larger areas. However there exist a few challenges as how to broaden its applications. A few suggestions for the future directions will be discussed below.

- 1) Improve fabrication process to achieve better tunability.

There can be several improvements in the fabrication: as shown by calculation result in Figure 24, replacing the magnetically soft nickel material by stronger magnetic materials with larger coercivity and permanent magnetic properties indicate promising improvement of tilt angle under the same external magnetic field condition. As the nickel plating solution is commercially available, other magnetic material plating techniques have also been shown [26]. Most permanent magnetic materials require a thermal annealing process after electroplating to enhance magnetic performance.

Fabricate micropillars with higher aspect ratio by an improved mold for electroplating is another way to improve magnetic bending torque. The challenge of electroplating with a photoresist mold is the photolithography process-limited aspect ratio. Typically for a thick photoresist, the aspect ratio for the holes is usually limited to 10:1. Moreover the stripping process for thick resist depends on a swelling induced lifting mechanism. The large stress imposed to nickel microstructures during photoresist swelling and lifting off usually result in the detachment of the plated metal from substrate surface. However, it is possible to use silicon as a mold for high aspect ratio electroplating. Electroplated micro structure with aspect ratios as high as 100 has been reported [27]. Thus, we anticipate a higher aspect ratio magnetic structure could be electroplated in the silicon mold for our study.

Better adhesion between the nickel pillars and the PDMS substrate is needed for microfluidic applications. Bonding between silica and PDMS has been reported to be very strong, and the technique has been commonly used in many PDMS microfluidic designs [28]. It was however difficult to visualize how the magnetic pillar detached from the PDMS surface. From the simulations, the largest stress occurred at the bonding interface between the silica-coated nickel pillars and the PDMS surface. To improve adhesion between PDMS and nickel pillar arrays, embedding a short pillar bottom into the PDMS layer might be a useful approach. It could also be possible that during silane CVD deposition, silane deposited into the gap between PDMS and nickel. In this way, the silane could possibly be a lubricant to reduce adhesion. Overall, more work is required to improve bonding between PDMS and nickel structures for the tunable surfaces to be applicable to microfluidic and phase change heat transfer systems.

Furthermore, scale down of the pillar geometry could bring opportunity in optical and biological applications. Optical applications usually demand a structural size on the order of the wavelength of visible lights. Therefore, submicron sized dynamic tunable surfaces will have great potential for these applications. However as the size becomes smaller the fabrication becomes more challenging. The fabrication for the tunable surfaces should be modified to fit the requirement of smaller size scales.

## 2) Develop an experimental platform to better control the applied field.

A stage that can more precisely control the magnetic field is needed to test the tilt angle of samples. One feasible design (Figure 28) would be attaching two strong magnets to the inner

surfaces of a yoke fixture. Connecting the yoke fixture with the two magnets separated with a small gap to a step motor which can have repeated rotational motions around the y-axis. The sample will be placed on a separate platform which rests in the small gap of the two magnets.

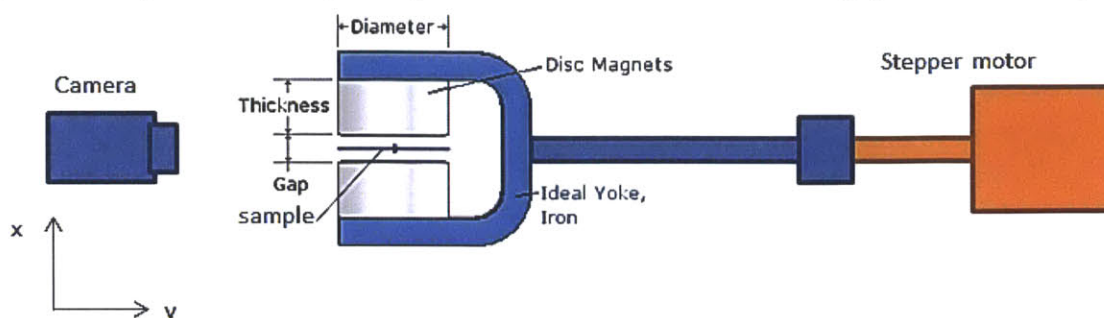


**Figure 28** Schematic of tilt angle testing stage.

- 3) Use the surface as a platform to manipulate water droplet transport and explore other applications.

Potential applications would be microfluidics and optical systems. Optical application would either require to scale down the sizes of the structure to control diffraction of the light or to apply reflective coating to the microstructure to tune light reflection direction. Microfluidics would also be an interesting field to work on, if we can achieve better fabrication to avoid defects and degradations. For example, the tunable structures can be applied to microchannels as fluid path switch to direct flow. They can also be used in condensation systems to potentially promote droplet removal rate. By controlling the field direction, we can direct fluid not only uni-directionally as suggested by Chu *et al.* [12] but actually direct fluid in any direction and dynamically control the fluid path, which greatly extended fluid manipulation capability.





## 6. Conclusion

This work shows a novel approach to create magnetically tunable surfaces, where the tilt angle of micropillar arrays can be controlled by an external magnetic field. Three different fabrication approaches were presented and compared in this work. The design of electroplated magnetic pillars attached to a soft substrate was pursued in detail. We successfully fabricated an  $8\text{ mm} \times 8\text{ mm}$  surface with uniform electroplated nickel micropillar arrays bonded on a PDMS substrate.

Characterization of the hysteresis loop verified the magnetic softness of the nickel material. It was only weakly magnetized when there was no external magnetic field. In light of this property, only dynamic tilt angle test was done to show deflection of the micropillars. Permanent magnetic materials show greater potential to extend the function of the microstructures to maintain a steady tilt angle.

With a field strength of 0.5 tesla and a field angle of  $60^\circ$ , a uniform  $10.5^\circ$  tilt angle of the pillar arrays was achieved. These tunable surface designs can serve as important device platforms in microfluidics, biological and optical applications. Future work will focus on building a system for precisely providing and controlled magnetic field, and using these surfaces to actively transport water droplets and spread the liquid film *via* pillar movement. Tunable surfaces with smaller size scale will have potential applications in biological and optical systems.

## Bibliography

- [1] R. Xiao and E. N. Wang, "Microscale Liquid Dynamics and the Effect on Macroscale Propagation in Pillar Arrays," *Langmuir*, vol. 27, no. 17, pp. 10360–10364, Sep. 2011.
- [2] J. Fu, Y.-K. Wang, M. T. Yang, R. A. Desai, X. Yu, Z. Liu, and C. S. Chen, "Mechanical regulation of cell function with geometrically modulated elastomeric substrates," *Nat. Methods*, vol. 7, no. 9, pp. 733–736, Sep. 2010.
- [3] K.-C. Park, H. J. Choi, C.-H. Chang, R. E. Cohen, G. H. McKinley, and G. Barbastathis, "Nanotextured Silica Surfaces with Robust Superhydrophobicity and Omnidirectional Broadband Supertransmissivity," *Acs Nano*, vol. 6, no. 5, pp. 3789–3799, May 2012.
- [4] R. Chen, M.-C. Lu, V. Srinivasan, Z. Wang, H. H. Cho, and A. Majumdar, "Nanowires for Enhanced Boiling Heat Transfer," *Nano Lett.*, vol. 9, no. 2, pp. 548–553, Feb. 2009.
- [5] K.-H. Chu, R. Enright, and E. N. Wang, "Structured surfaces for enhanced pool boiling heat transfer," *Appl. Phys. Lett.*, vol. 100, no. 24, pp. 241603–241603–4, Jun. 2012.
- [6] S. Kim, H. D. Kim, H. Kim, H. S. Ahn, H. Jo, J. Kim, and M. H. Kim, "Effects of nano-fluid and surfaces with nano structure on the increase of CHF," *Exp. Therm. Fluid Sci.*, vol. 34, no. 4, pp. 487–495, May 2010.
- [7] K.-H. Chu, Y. Soo Joung, R. Enright, C. R. Buie, and E. N. Wang, "Hierarchically structured surfaces for boiling critical heat flux enhancement," *Appl. Phys. Lett.*, vol. 102, no. 15, pp. 151602–151602–4, Apr. 2013.
- [8] D. Li, G. S. Wu, W. Wang, Y. D. Wang, D. Liu, D. C. Zhang, Y. F. Chen, G. P. Peterson, and R. Yang, "Enhancing Flow Boiling Heat Transfer in Microchannels for Thermal Management with Monolithically-Integrated Silicon Nanowires," *Nano Lett.*, vol. 12, no. 7, pp. 3385–3390, Jul. 2012.
- [9] C.-J. Kuo and Y. Peles, "Local measurement of flow boiling in structured surface microchannels," *Int. J. Heat Mass Transf.*, vol. 50, no. 23–24, pp. 4513–4526, Nov. 2007.
- [10] N. Miljkovic, R. Enright, Y. Nam, K. Lopez, N. Dou, J. Sack, and E. N. Wang, "Jumping-Droplet-Enhanced Condensation on Scalable Superhydrophobic Nanostructured Surfaces," *Nano Lett.*, vol. 13, no. 1, pp. 179–187, Jan. 2013.
- [11] J. A. Weibel, S. V. Garimella, and M. T. North, "Characterization of evaporation and boiling from sintered powder wicks fed by capillary action," *Int. J. Heat Mass Transf.*, vol. 53, no. 19–20, pp. 4204–4215, Sep. 2010.
- [12] K.-H. Chu, R. Xiao, and E. N. Wang, "Uni-directional liquid spreading on asymmetric nanostructured surfaces," *Nat. Mater.*, vol. 9, no. 5, pp. 413–417, May 2010.
- [13] N. A. Malvadkar, M. J. Hancock, K. Sekeroglu, W. J. Dressick, and M. C. Demirel, "An engineered anisotropic nanofilm with unidirectional wetting properties," *Nat. Mater.*, vol. 9, no. 12, pp. 1023–1028, Dec. 2010.
- [14] "MEMS Based Structurally Tunable Metamaterials at Terahertz Frequencies - Springer."
- [15] Q. Zhou, W. D. Ristenpart, and P. Stroeve, "Magnetically Induced Decrease in Droplet Contact Angle on Nanostructured Surfaces," *Langmuir*, vol. 27, no. 19, pp. 11747–11751, Oct. 2011.
- [16] X. He, M. Aizenberg, O. Kuksenok, L. D. Zarzar, A. Shastri, A. C. Balazs, and J. Aizenberg, "Synthetic homeostatic materials with chemo-mechano-chemical self-regulation," *Nature*, vol. 487, no. 7406, pp. 214–218, Jul. 2012.

- [17] N. Sniadecki, A. Anguelouch, M. Yang, C. Lamb, Z. Liu, S. Kirschner, Y. Liu, D. Reich, and C. Chen, "Magnetic microposts as an approach to apply forces to living cells," *Dep. Pap. Be*, Jul. 2007.
- [18] F. Mugele and J.-C. Baret, "Electrowetting: from basics to applications," *J. Phys. Condens. Matter*, vol. 17, no. 28, p. R705, Jul. 2005.
- [19] D. Huh, A. H. Tkaczyk, J. H. Bahng, Y. Chang, H.-H. Wei, J. B. Grotberg, C.-J. Kim, K. Kurabayashi, and S. Takayama, "Reversible Switching of High-Speed Air-Liquid Two-Phase Flows Using Electrowetting-Assisted Flow-Pattern Change," *J. Am. Chem. Soc.*, vol. 125, no. 48, pp. 14678–14679, Dec. 2003.
- [20] F. Hua, T. Cui, and Y. M. Lvov, "Ultrathin Cantilevers Based on Polymer-Ceramic Nanocomposite Assembled through Layer-by-Layer Adsorption," *Nano Lett.*, vol. 4, no. 5, pp. 823–825, May 2004.
- [21] R. T. Olsson, M. A. S. A. Samir, G. Salazar-Alvarez, L. Belova, V. Ström, L. A. Berglund, O. Ikkala, J. Nogués, and U. W. Gedde, "Making flexible magnetic aerogels and stiff magnetic nanopaper using cellulose nanofibrils as templates," *Nat. Nanotechnol.*, vol. 5, no. 8, pp. 584–588, Aug. 2010.
- [22] Z. Gu, S. Huang, and Y. Chen, "Biomolecular Nanopatterning by Magnetic Electric Lithography," *Angew. Chem. Int. Ed.*, vol. 48, no. 5, pp. 952–955, 2009.
- [23] D. Armani, C. Liu, and N. Aluru, "Re-configurable fluid circuits by PDMS elastomer micromachining," in *Twelfth IEEE International Conference on Micro Electro Mechanical Systems, 1999. MEMS '99*, 1999, pp. 222–227.
- [24] Y. Nam, S. Sharratt, C. Byon, S.-J. Kim, and Y. S. Ju, "Fabrication and Characterization of the Capillary Performance of Superhydrophilic Cu Micropost Arrays," *J. Microelectromechanical Syst.*, vol. 19, no. 3, pp. 581–588, 2010.
- [25] K. E. Plass, M. A. Filler, J. M. Spurgeon, B. M. Kayes, S. Maldonado, B. S. Brunschwig, H. A. Atwater, and N. S. Lewis, "Flexible Polymer-Embedded Si Wire Arrays," *Adv. Mater.*, vol. 21, no. 3, pp. 325–328, 2009.
- [26] D. P. Arnold and N. Wang, "Permanent Magnets for MEMS," *J. Microelectromechanical Syst.*, vol. 18, no. 6, pp. 1255–1266, 2009.
- [27] G. Sun, J. I. Hur, X. Zhao, and J. Y. Kim, "Fabrication of Very-High-Aspect-Ratio Micro Metal Posts and Gratings by Photoelectrochemical Etching and Electroplating," *J. Microelectromechanical Syst.*, vol. 20, no. 4, pp. 876–884, 2011.
- [28] J. Friend and L. Yeo, "Fabrication of microfluidic devices using polydimethylsiloxane," *Biomicrofluidics*, vol. 4, no. 2, Mar. 2010.

## Appendix: Calculation of deflection angle of microstructured surfaces fabricated from bacteria cellulose nanofibrils embedded with magnetic nanoparticles

1. Torque exerted on the magnetic pillar:

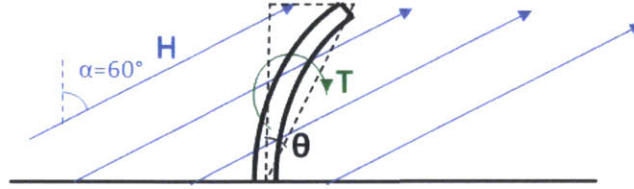


**Figure A1.** Schematic diagram of a magnetic pillar inside magnetic field

Due to magnetization, magnetic flux density inside the pillar

$$\mathbf{B} = \mu_0(\mathbf{H} + \mathbf{M})$$

where  $\mathbf{M}$  is magnetization, material response to the external field  $\mathbf{H}$ . If we magnetize the material in its axial direction, then the direction of  $\mathbf{M}$  of the pillar is also in its axial direction.

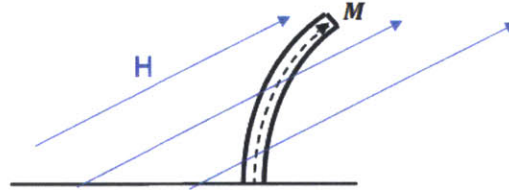


**Figure A2.** Direction of  $\mathbf{M}$  and  $\mathbf{H}$

$\mathbf{M}$  can be acquired from Olsson et al.'s experiment<sup>[1]</sup>, which are illustrated in figure 3<sup>[1]</sup>. When external magnetic field  $\mathbf{H}$  is zero, the material is not magnetized and  $\mathbf{M}$  is also zero. Before applying the external magnetic field  $\mathbf{H}$  in the direction shown in figure 1 and 2, we apply  $\mathbf{H}$  in the axial direction of the pillar and drive the Magnetization of the pillar to its saturation point. Then  $\mathbf{H}$  is decreased and direction of which is also changed as shown in figure 1 and 2 in order to deflect the pillar. In this case M-H relationship obeys the upper line (red line) of the hysteresis loop in shown in figure A3.

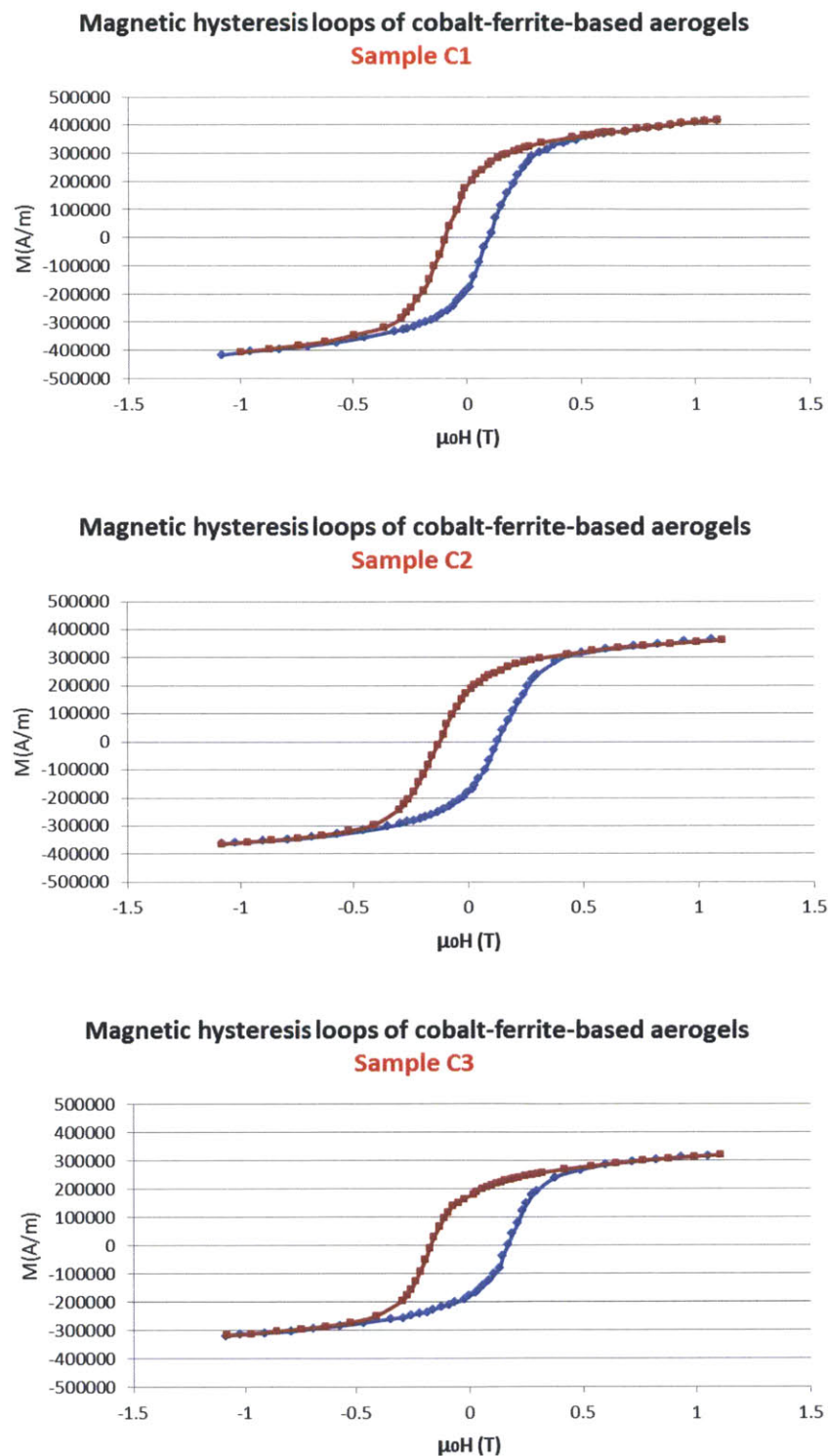


**Figure A3.** Magnetic hysteresis loops of cobalt-ferrite-based aerogels. Sample C1 to C3 has FeSO<sub>4</sub>/CoCl<sub>2</sub> salts molar ratio of 0.1, 0.165 and 0.2 respectively



The magnetic torque is

$$\begin{aligned}
T &= xV\mathbf{M} \times \mathbf{B} \\
&= xV\mathbf{M} \times \mu_0(\mathbf{H} + \mathbf{M}) \\
&= xV\mathbf{M} \times \mu_0\mathbf{H} + xV\mathbf{M} \times \mu_0\mathbf{M} \\
&= xVM\mu_0H\sin(\alpha - \theta) + 0 \\
&= \frac{\pi}{4}d^2hxM\mu_0H\sin(\alpha - \theta)
\end{aligned} \tag{1}$$

where  $V$  is the volume of the pillar,  $x$  is volume fraction of magnetic composite in the pillar,  $h$  is height of the pillar and  $d$  is the diameter of the pillar.

2. Deflection and deflection angle of the pillar:

2.1 Deflection for small angles

When deflection is small, the following formula can be applied to the model:

$$\begin{aligned}
\delta &= \frac{M_0 \frac{h}{2} \left(2h - \frac{h}{2}\right)}{2EI} \\
&= \frac{3M_0h^2}{8EI}
\end{aligned}$$

where  $M_0$  is moment/torque on the pillar,  $I = \frac{\pi}{64}d^4$

So  $\theta$  is approximately:

$$\theta = \frac{\delta}{h} = \frac{3M_0h}{8EI}$$

When the system is steady,  $T = M_0$ , that is,

$$\begin{aligned}
\theta &= \frac{3 \times \frac{\pi}{4}d^2hxM\mu_0H\sin(\alpha - \theta)h}{8E \frac{\pi}{64}d^4} \\
&= \frac{6h^2xM\mu_0H\sin(\alpha - \theta)}{Ed^2}
\end{aligned}$$

The above equation can be rewritten as:

$$\theta = k\sin(\alpha - \theta) \tag{2}$$

$$\text{where } k = \frac{6h^2xM\mu_0H}{Ed^2}$$

$\theta$  can be derived from equation (2) numerically. Equation (2) shows that the deflection angle is a function of  $h/d$ , which means  $\theta$  will remain the same when  $h$  and  $d$  changes simultaneously. Parameters for this model is listed in Table 1 and Table 2. Figure 4 and Figure 5 shows the

calculated results for small deflection angles. However it should be noticed that equation (2) is not accurate for large deflections.

**Table A1.** Parameters for the magnetic aerogel (derived from [1])

Parameter	description	Sample C1	Sample C2	Sample C3
$C$ (mol dm <sup>-3</sup> )	Molar ratio	0.1	0.165	0.2
$w$	Weight fraction	70.9%	78.9%	93.6%
$x$	Volume fraction	59%*0.7%	63%*2.7%	85%*5.7%
$M_s$ (kA m <sup>-1</sup> )	Saturation magnetization	400	350	300
$\mu_0 H_c$ (mT)	Coercivity	95	130	170
$E$ (MPa)	Young's modulus	0.15	0.15	0.15

**Table A2.** Other parameters for the model (Adjustable)

Parameter (SI unit)	description	value
$H$ (A/m)	External magnetic field intensity	Adjustable
$M$	Magnetization of material	From Fig 2d
$\mu_0$ (Hengry/m)	constant	$4\pi*10^{-7}$
$B$ (tesla,T)	Magnetic flux density	$B = \mu_0(H + M)$
$\alpha$ (Degree)	Angle between $H$ and the un-deflected pillar	60
$\theta$ (Degree)	Deflection angle	tunable
$V$ (m <sup>3</sup> )	Volume of the magnetic pillar	tunable
$h$	Height of the pillar	tunable
$d$	Diameter of cross-section of the pillar	tunable

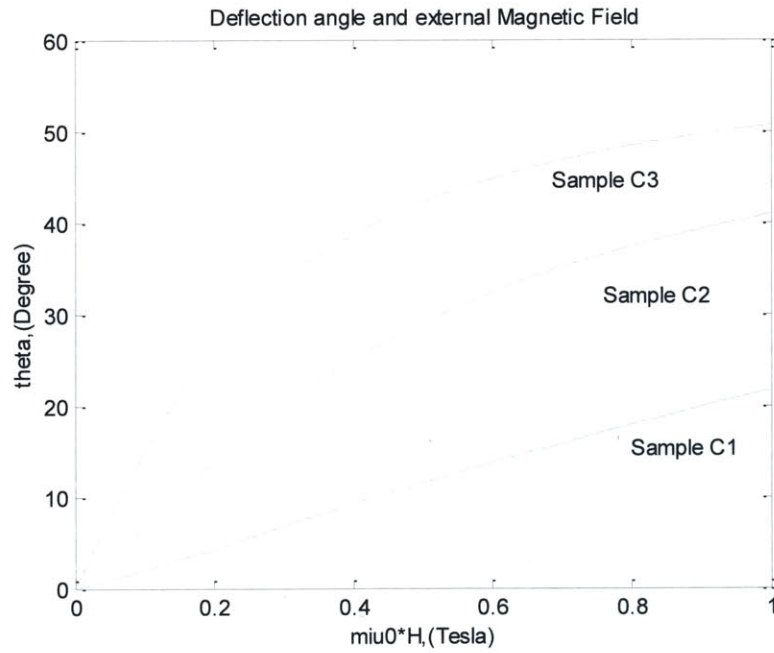


**Figure A4.** Deflection angle vs. external magnetic field when  $h/d = 3$  and deflection angle is small

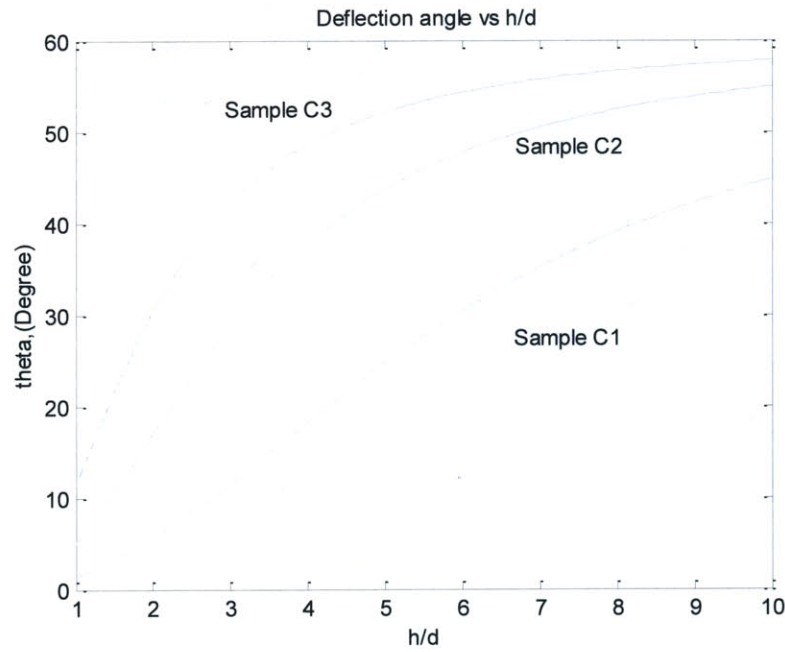


**Figure A5.** Deflection angle vs.  $h/d$  when external magnetic field is 0.5 tesla and deflection angle is small

## 2.2 Deflection angle for both small and large angles

When deflection is large, the approximation may not be applied to the case. Here we try to find the exact expression for deflection of the pillar.

Exact Expression for the curvature of the pillar is

$$\frac{v''}{(1+(v')^2)^{3/2}} = \frac{F_x x}{EI} \quad (3)$$

where  $v$  is deflection which is a function of  $x$ ,  $F_x$  is the magnetic force acting on the pillar in the x-axial component.

Assumption of small rotations is equivalent to disregarding  $(v')^2$  in comparison to one. Equation (3) can be used for the curvature whenever the slopes are large.

Euler solved the differential equation of the deflection curve for large deflections.<sup>[2]</sup> The result of equation (3) is

$$\delta = \frac{2F_x h^3}{6EI + 3F_x h^2} \quad (4)$$

So the deflection angle  $\theta$  defined in figure 1 should be

$$\theta = \arcsin\left(\frac{\delta}{h}\right) = \arcsin\left(\frac{2F_x h^2}{6EI + 3F_x h^2}\right) \quad (5)$$

When system is steady,

$$F_x = \frac{T \cos \alpha}{h \sin(\alpha - \theta)} \quad (6)$$

Subscribe equation (1) and (6) into equation (5) we get

$$\theta = \arcsin\left(\frac{16\pi x M \mu_0 H \cos \alpha \left(\frac{h}{d}\right)^2}{3\pi E + 24\pi x M \mu_0 H \left(\frac{h}{d}\right)^2}\right) \quad (7)$$

The more general equation (7) also indicates that deflection angle is also only relevant with  $h/d$ . Using the same parameters listed in Table 1 and Table 2, we can get deflection angle from equation (7).

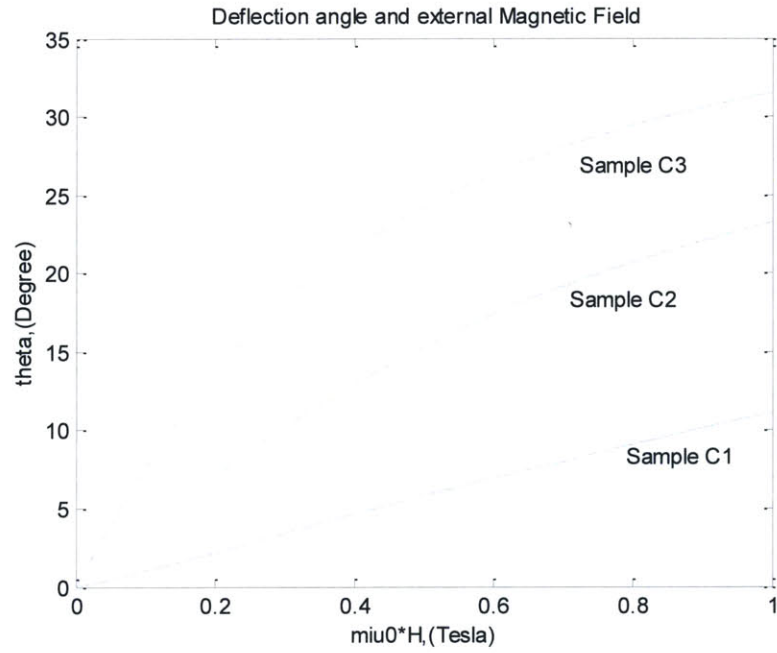


Figure A6. Deflection angle vs. external magnetic field when  $h/d = 3$

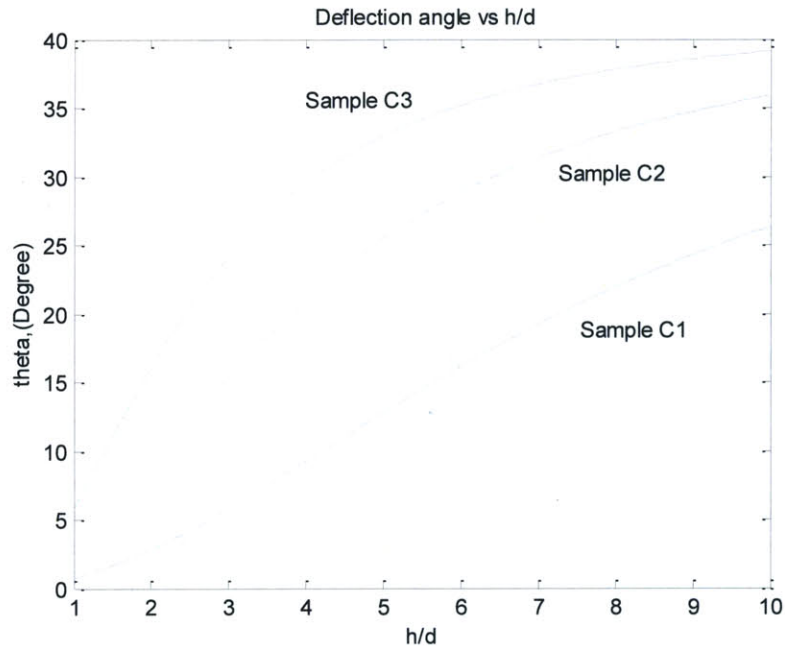


Figure A7. Deflection angle vs.  $h/d$  when external magnetic field is 0.5 tesla

### 3. Discussion

We first set up a model that is suitable for small deflection angles. The calculated result shows that deflection angle is relatively large (Figure 4, 5). Then the model is extended to suit



the more general case where deflection angle can be large. In the more general case deflection angle are much less than the former model when deflection angle is relatively large (Figure 6, 7).

In both models, deflection angle is only relevant with the ratio of height and cross-section diameter of the pillar ( $h/d$ ). It is not relevant with the absolute value of either height or cross-section diameter. This is a significant feature because it allows us to make bigger pillars while still achieving the same deflection angle in the same external magnetic field. However the spreading behavior of water is relevant with pillar height. (Refer to *Unidirectional liquid spreading on asymmetric nanostructured surfaces*)

The three samples shows that the more concentration of the  $\text{FeSO}_4/\text{CoCl}_2$  salts added into the nanofibril, the more easily it can be deflected. From figure 6 it can be observed that we can make magnetic aerogel pillar with characters of sample C3, in order to achieve a deflection angle of  $10^\circ$  with an external magnetic field of 0.15 T (while  $h/d = 3$ )

Deflection angle tend to increase when  $h/d$  increases. However the increasing trend slows down when  $h/d$  is larger than 5. Specially, with Sample C3, the difference of deflection angles when  $h/d=5$  and 10 is only around  $7^\circ$ . This is also an important feature because when it is hard to make aerogel pillar with  $h/d>5$ , it's also unnecessary.

Two important factors are still not considered here:

- a) The influence of polymer coating outside of the magnetic pillar is not considered.
- b) Interaction of pillar and water is not considered.

When those two factored are considered further in this model, deflection angles should be less than Figure 6 and 7.